ARTICLES
https://doi.org/10.1038/s41477-021-00889-y

nature plants

HIGH CROSSOVER RATE1 encodes PROTEIN PHOSPHATASE X1 and restricts meiotic crossovers in *Arabidopsis*

Divyashree C. Nageswaran[1,3], Jaeil Kim[2,3], Christophe Lambing[1], Juhyun Kim[2], Jihye Park[2], Eun-Jung Kim[2], Hyun Seob Cho[2], Heejin Kim[2], Dohwan Byun[2], Yeong Mi Park[2], Pallas Kuo[1], Seungchul Lee[2], Andrew J. Tock[1], Xiaohui Zhao[1], Ildoo Hwang[2], Kyuha Choi[1,2] ✉ and Ian R. Henderson[1] ✉

Meiotic crossovers are tightly restricted in most eukaryotes, despite an excess of initiating DNA double-strand breaks. The majority of plant crossovers are dependent on class I interfering repair, with a minority formed via the class II pathway. Class II repair is limited by anti-recombination pathways; however, similar pathways repressing class I crossovers have not been identified. Here, we performed a forward genetic screen in *Arabidopsis* using fluorescent crossover reporters to identify mutants with increased or decreased recombination frequency. We identified *HIGH CROSSOVER RATE1* (*HCR1*) as repressing crossovers and encoding PROTEIN PHOSPHATASE X1. Genome-wide analysis showed that *hcr1* crossovers are increased in the distal chromosome arms. MLH1 foci significantly increase in *hcr1* and crossover interference decreases, demonstrating an effect on class I repair. Consistently, yeast two-hybrid and in planta assays show interaction between HCR1 and class I proteins, including HEI10, PTD, MSH5 and MLH1. We propose that HCR1 plays a major role in opposition to pro-recombination kinases to restrict crossovers in *Arabidopsis*.

Meiosis is a specialized type of cell division occurring in eukaryotes, in which a single round of DNA replication is coupled to two rounds of chromosome segregation, generating haploid cells that can undergo sexual fusion[1,2]. During meiotic prophase I, homologous chromosomes pair and undergo programmed recombination, which can produce reciprocal crossovers between chromosomes[1,2]. Meiotic recombination and chromosome segregation cause the haploid gametes to be genetically mosaic[1,2]. As a consequence, sex has a profound effect on genetic variation and adaptation[1,2].

Meiotic recombination initiates with the formation of DNA double-strand breaks (DSBs), via the conserved topoisomerase-related protein SPO11[1,2]. In plants, SPO11-1 and SPO11-2 form a heterotetramer with MEIOTIC TOPOISOMERASE VIB-LIKE (MTOPVIB) to generate meiotic DSBs[3–5]. Mutation of *spo11-1*, *spo11-2* or *mtopvib* prevents homologue pairing, causing univalent segregation at metaphase I and aneuploid gametes in *Arabidopsis*[3–5]. Meiotic DSBs are resected to generate single-stranded DNA (ssDNA) that is bound by the RecA-related proteins DMC1 and RAD51[6]. DMC1–RAD51 nucleofilaments mediate interhomologue strand invasion to form displacement loops[2,6]. In wild-type *Arabidopsis*, around 150–250 DSB-associated foci are evident along the meiotic chromosome axis when DMC1, RAD51, RPA1a and γH2A.X are immunostained during early meiotic prophase I[2,7]. In wild-type *Arabidopsis*, only around ten of these DSBs are ultimately repaired as interhomologue crossovers[2,8]. The remaining strand invasion events are disassembled by non-crossover pathways, which include FANCM, RECQ4A, RECQ4B and FIGL1[2,9]. Meiotic DSBs may also be repaired using the sister chromatid[2,10].

In plants, the major pathway generating crossovers is termed class I (also known as the ZMM pathway)[2]. Class I crossovers show interference, meaning they are more widely spaced than expected by chance[11]. In plants, around 80–85% of crossovers are dependent on the class I pathway, which includes MSH4, MSH5, ZIP4, SHOC1, PTD, HEI10, HEIP1, MER3, MLH1 and MLH3[2,12]. The class I pathway functions to stabilize interhomologue joint molecules and promotes crossover resolution via double Holliday junctions[13]. Within this pathway; MSH4 and MSH5 form the MutSγ heterodimer that associates with meiotic chromosomes and stabilizes interhomologue joint molecules[13], SHOC1 and PTD form a catalytically inactive XPF–ERCC1 endonuclease-related complex that has affinity for joint molecules[13], HEI10 belongs to a family of ubiquitin and SUMO E3 ligases[13], MER3 is a DNA helicase[14] and MLH1 and MLH3 form the MutLγ heterodimer, which has endonuclease activity[13]. A minority (about 15–20%) of crossovers in plants are non-interfering and dependent on the class II pathway[2]. In anti-recombination pathway mutants, for example *recq4a recq4b*, there are large increases in the numbers of class II crossovers[15,16].

Progression of the meiotic cell cycle and recombination are regulated by multiple protein kinase pathways, whose targets include DSB proteins, the class I pathway and the chromosome axis[17]. For example, cell division kinase CDKA;1 promotes class I crossovers in *Arabidopsis*, and directly targets MLH1 in vitro[18]. In mammals and budding yeast, the ATM/ATR (also known as Mec1/Tel1) DNA-damage kinases are activated by meiotic DSBs, and mediate feedback signalling on recombination in *cis* and *trans*[19–21]. Zip3, a HEI10 orthologue, has been shown to be a target of Mec1/Tel1 in budding yeast[22]; it is antagonized by the PPH3–PP4 protein

[1]Department of Plant Sciences, University of Cambridge, Cambridge, UK. [2]Department of Life Sciences, Pohang University of Science and Technology, Pohang, Republic of Korea. [3]These authors contributed equally: Divyashree C. Nageswaran, Jaeil Kim. ✉e-mail: kyuha@postech.ac.kr; irh25@cam.ac.uk

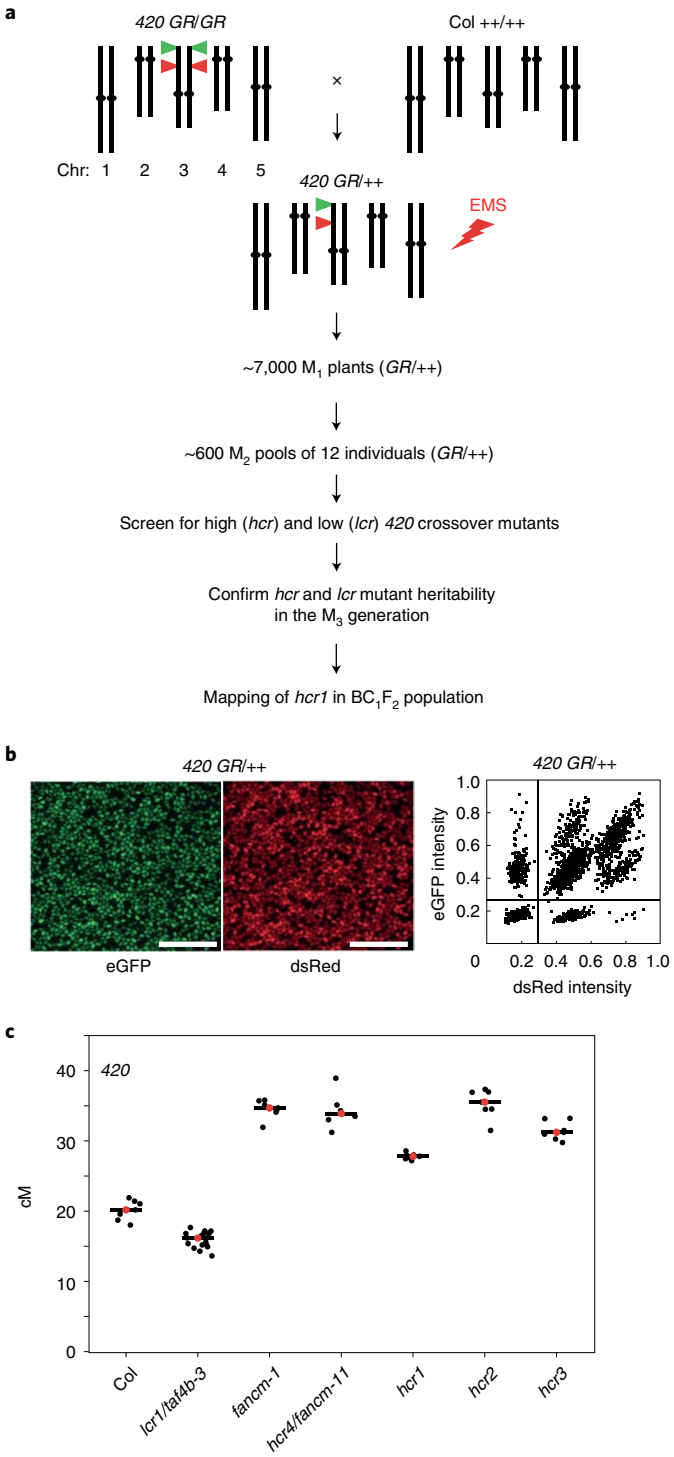

Fig. 1 | A forward genetic screen for mutants with changed *420* crossover frequency. a, Schematic of a forward genetic screen for identifying high (*hcr*) or low (*lcr*) crossover mutants, using the *420* FTL crossover reporter interval (green and red triangles on chromosome 3). *420/++* seed were treated with EMS and the subsequent steps were followed to identify the *hcr1* mutant. **b**, Representative fluorescent micrographs of *420/++* seeds. Scale bars, 5 mm. A representative plot of red (dsRed) and green (eGFP) fluorescence values from *420/++* seed is shown. Vertical and horizontal lines indicate thresholds for colour:non-colour classifications used for crossover frequency estimation. **c**, *420* crossover frequency (cM) in wild type, *fancm*, *hcr* and *lcr* mutants. Red dots and black horizontal bars represent the mean.

phosphatase complex[22]. The Dbf4/Drf1-dependent kinase Cdc7 complex (DDK) phosphorylates a MSH4 degron to stabilize its association with recombination sites in budding yeast[23]. Proteins of the chromosome axis, including ASY1 and REC8, are also extensively phosphorylated during meiosis[24,25]. How protein kinases and phosphatases are balanced to control meiotic crossovers in plants remains unknown.

To identify factors that control meiotic recombination, we performed a forward genetic screen using a fluorescent crossover reporter. This screen identified the *high crossover rate1* (*hcr1*) mutant in *PROTEIN PHOSPHATASE X1*, which functions in the nuclear PP4 protein phosphatase complex[26–28]. Crossovers increased most strongly in distal euchromatic regions in *hcr1* plants and the strength of interference decreased. As MLH1 foci significantly increase in *hcr1*, this shows that HCR1 represses the class I crossover pathway. Consistently, yeast two-hybrid (Y2H) and co-immunoprecipitation assays show that HCR1 interacts with the class I proteins HEI10, PTD, MSH5 and MLH1. We also observed Y2H interactions between HCR1 and chromosome axis proteins, DSB factors and recombinases, indicating a potential broader regulatory role during meiosis. We propose that HCR1/PPX1–PP4 phosphatases act in opposition to pro-recombination kinase pathways, to limit crossovers in *Arabidopsis*.

Results

A forward genetic screen for mutants with altered meiotic crossover frequency. To isolate factors controlling meiotic crossover frequency we performed a forward genetic screen in *Arabidopsis thaliana* (Fig. 1a). We made use of fluorescent reporters of crossover frequency, which consist of linked fluorescent tagged lines (FTL)/Col traffic lines (CTL) T-DNA insertions expressing fluorescent proteins of different colours in the seed (under control of the *NapA* promoter) or pollen (under the *LAT52* promoter)[29–31] (Fig. 1b). When FTLs are hemizygous, inheritance of fluorescence can be used to score crossover frequency within the interval defined by the T-DNAs[29–32] (Fig. 1b). We selected the *420* FTL for mutagenesis, which defines a 5.1 megabase interval located in the left sub-telomeric region of chromosome 3[30,32] (Fig. 1a,b). *420* was selected for mutagenesis, as crossover frequency in this region is known to be sensitive to multiple recombination and chromatin pathways[32–36].

We generated approximately 10,000 *420/++* hemizygous seeds by crossing, and used them for ethyl methanesulfonate (EMS) mutagenesis (Fig. 1a). From these seeds, about 7,000 M_1 plants were grown and M_2 seeds were collected (Fig. 1a). The seeds from 12 independent M_1 plants were combined to generate about 600 M_2 pools (Fig. 1a), and seeds within these pools were pre-selected to be red–green fluorescent (*420/++* hemizygous). Approximately 150 pre-selected seeds were grown from each M_2 pool and allowed to self-fertilize (Fig. 1a). Seeds from individual M_2 plants were used to score crossover frequency within *420* (Fig. 1a,b). In our growth conditions, *420* in self-fertilized wild-type Col/Col inbred plants shows a mean crossover frequency of 20.19 cM (s.d. 1.43 cM) (Fig. 1c and Supplementary Table 1). In total, 2,883 M_2 individuals were screened and the majority (81.4%) showed *420* crossover frequency within the range of 18–22 cM (Extended Data Fig. 1). Nineteen putative high or low crossover-frequency mutants were self-fertilized and M_3 progeny were tested for *420* crossover frequency, of which 5 were confirmed to show a heritable recombination phenotype in the next generation (Fig. 1a).

We identified four mutants with high- and one with low *420* crossover frequency (Fig. 1c and Supplementary Table 1), which we term *high crossover rate1* (*hcr1*), *hcr2*, *hcr3*, *hcr4* and *low crossover rate1* (*lcr1*). The *hcr4* mutant was shown to be allelic to *fancm* (Extended Data Fig. 2 and Supplementary Table 1), a known repressor of class II crossovers[37]. The *hcr4* (*fancm-11*) allele is caused by a

non-synonymous amino acid substitution (G540S) in the conserved SF2 helicase domain and shows a comparable effect on *420* crossover frequency to the *fancm-1* allele[37] (Fig. 1c, Extended Data Fig. 2 and Supplementary Table 1). We observed that *lcr1* was allelic with the *taf4b* mutant (*taf4b-3*) (Extended Data Fig. 2 and Supplementary Table 2), which was previously shown to promote crossovers in the distal chromosome arms[34]. In this study we focused on identification and functional characterization of *hcr1* (Fig. 1c).

To map the *hcr1* mutation, we produced a BC_1F_2 mapping population by backcrossing M_3 *hcr1 420* (*GR/GR*) plants to wild type (Col) (Figs. 1a and 2a). The *420* crossover frequency was not significantly different between *hcr1*/+ BC_1F_1 and wild type, showing that *hcr1* is recessive (Welch's *t*-test, $P=0.241$) (Fig. 2a and Supplementary Table 3). The *hcr1*/+ *420*/++ BC_1 hybrid plants were then self-fertilized to generate a 300-individual BC_1F_2 population, which was scored for *420* crossover frequency (Fig. 1a). Material from the 60 BC_1F_2 plants with the highest *420* crossover frequency was pooled and used for genomic DNA extraction and short-read sequencing (Fig. 2a). We applied the SHORE[38] mapping pipeline to identify candidate EMS mutations in the high crossover BC_1F_2 sequencing library (Fig. 2b). The candidate mutation with highest frequency was a G-to-A substitution in a splice donor site of the third intron of At4g26720, which encodes PROTEIN PHOSPHATASE X1 (PPX1)[28] (Fig. 2b,c and Supplementary Table 4).

***HIGH CROSSOVER RATE1* encodes PROTEIN PHOSPHATASE X1.** We used PCR with reverse transcription (RT–PCR) to amplify and sequence *PPX1* mRNA from *hcr1* plants, revealing retention of intron 3, causing a premature stop codon (Fig. 2c and Extended Data Fig. 3). The stop codon is predicted to truncate PPX1 (retaining 143 of 305 residues) and remove conserved metal-binding histidine residues in the C-terminal region[39] (Fig. 2c and Extended Data Fig. 4a). However, the truncated protein has the potential to encode three of four conserved PPX1 catalytic motifs (GDXHG, GDXVDRG and GNHE) in the N-terminal region[39] (Fig. 2c and Extended Data Fig. 4a). PPX1 is the catalytic subunit of the hetero-multimeric PP4 serine/threonine protein phosphatase complex, which includes two additional regulatory subunits (PP4R2 and PP4R3)[40] (Fig. 2d). PP4 complexes have multiple roles in mitotic and meiotic DNA recombination and repair in diverse eukaryotes[26,27,41–48].

To demonstrate whether the splice acceptor mutation in *PPX1* causes the *hcr1 420* crossover phenotype, we performed a complementation test (Fig. 2f and Supplementary Table 5). A 4,515-bp genomic fragment containing the *PPX1* gene was amplified by PCR from wild type (Col) and inserted into an *Agrobacterium* binary vector and used to transform *hcr1 420*/++ plants. We observed that the *hcr1* plants transformed with *PPX1*, but not those transformed with empty vector, showed *420* crossover frequency not significantly different to the wild type (Welch's *t*-test, $P=0.357$) (Fig. 2f and Supplementary Table 5). We obtained a second T-DNA insertion (GK_651B07) mutation in *PPX1*, located in the 5′-untranslated region (UTR), which we term *hcr1-2*, and term the EMS allele *hcr1-1* (Fig. 2c,g and Supplementary Table 6). We measured *420* crossover frequency in *hcr1-2* homozygotes and observed a significant increase compared to wild type (Welch's *t*-test, $P=5.43\times10^{-8}$) (Fig. 2g and Supplementary Table 6), although the phenotype was weaker than that of *hcr1-1* mutants. We crossed *hcr1-1* with *hcr1-2* to generate *hcr1-1/hcr1-2* F_1 hybrids, which showed significantly higher *420* crossovers compared with wild type, demonstrating allelism (Welch's *t*-test, $P=4.91\times10^{-10}$) (Fig. 2g and Supplementary Table 6). Together, these genetic data identify *PPX1* as *HCR1*.

The *Arabidopsis* genome encodes a second PP4C catalytic subunit gene, *PPX2* (At5g55260), which shows 93.8% amino acid sequence identity to PPX1[49–51] (Fig. 2d and Extended Data Fig. 4). Functional redundancy between *Arabidopsis PPX1* and *PPX2* has been observed[28]. We obtained a T-DNA insertion in *PPX2* (GK_488H09), which disrupts mRNA expression, but did not observe a significant effect on *420* crossovers, compared to wild type (Welch's *t*-test, $P=0.119$) (Fig. 2h, Extended Data Fig. 3a,b and Supplementary Table 7). However, *hcr1-2 ppx2-1* double mutants showed a significant increase in *420* crossovers compared with *hcr1-2* (Welch's *t*-test, $P=1.42\times10^{-4}$) (Fig. 2h and Supplementary Table 7). We also crossed *hcr1-1* with a second *ppx2* T-DNA insertion allele (*ppx2-2*) but did not obtain any *hcr1-1 ppx2-2* double mutants in the F_2 generation. As the siliques of *hcr1-1*/+ *ppx2-2*/+ plants contained aborted seeds that were not seen in wild-type controls, these data suggest that the double mutant is embryo or seedling lethal (Extended Data Fig. 3d–f). *Arabidopsis* encodes a single gene for the PP4R2 regulatory subunit (At1g17070), and we obtained a T-DNA insertion that disrupts mRNA expression of this gene (Extended Data Fig. 3a,b). We observed that *pp4r2* shows a significant increase in *420* crossover frequency, compared to wild type (Welch's *t*-test, $P=4.24\times10^{-5}$), with a similar phenotypic strength to *hcr1-2* (Fig. 2h and Supplementary Table 7). As *pp4r2* mutants are viable, this indicates that the T-DNA insertion is likely to be hypomorphic. Together, these results are consistent with HCR1/PPX1 and PPX2 acting in PP4 complexes with PP4R2 to repress meiotic crossovers in *Arabidopsis*. We also note that recent mass spectroscopy data from *Arabidopsis* has confirmed the presence of HCR1/PPX1, PPX2, PP4R2L and PP4R3A complexes in vivo[28].

Meiosis-specific knockdown of *HCR1/PPX1* and *PPX2* using meiMIGS. Our genetic analysis indicates functional redundancy between *PPX1* and *PPX2* (Fig. 2h). This is consistent with null *ppx1 ppx2* double mutants causing severe developmental phenotypes that are not observed in the single mutants[28]. Therefore, we sought to silence both *PPX1* and *PPX2* specifically during meiosis. For this purpose, we adapted miRNA-induced gene silencing (MIGS) for use during meiosis[52]. In MIGS constructs, a microRNA173 (miR173) target site is inserted upstream of target transcript sequences[52]. Transcript cleavage of the fusion RNA by endogenous miR173 is an efficient trigger of 22-nucleotide *trans*-acting siRNAs, which act to silence endogenous gene transcripts that share sequence homology in *trans*[52]. To drive MIGS specifically during meiosis (meiMIGS), we expressed miRNA173-target *PPX1* and *PPX2* gene fusions from the *DMC1* promoter[53] (Fig. 3a). We measured

Fig. 2 | *HIGH CROSSOVER RATE1* encodes PROTEIN PHOSPHATASE X1. a, *420* crossover frequency (cM) in wild-type, *hcr1-1*, *hcr1-1*/+ and high recombination *hcr1-1* BC_1F_2 individuals used for DNA extraction and mapping by sequencing. **b**, Allele frequency of EMS mutations (red) identified by SHOREmap in high recombination *hcr1-1* BC_1F_2 individuals. The blue horizontal line indicates an allele frequency of 0.5. The *hcr1-1* candidate region and mutations are highlighted on chromosome 4 with grey shading. **c**, Top: the *HCR1/PPX1* gene, with exons shown as boxes (black, coding DNA sequence; grey, UTR) and the red asterisk indicating the position of the *hcr1-1* substitution. The *hcr1-2* T-DNA insertion (triangle) is located in the 5′-UTR (triangle). Bottom: the HCR1/PPX1 protein, showing the serine/threonine protein phosphatase domain (red), catalytic motifs (blue) and the position of the premature stop codon (red asterisk) caused by *hcr1-1*. aa, amino acids. **d**, A representation of the PP4 phosphatase complex with PP4C, PP4R2 and PP4R3 subunits. Cognate *Arabidopsis* homologous genes are listed. **e**, PPX/PP4C neighbour-joining phylogenetic tree based on an alignment of amino acid sequences. The scale bar represents the number of changes per amino acid position. **f**, As in **a**, but showing *420* crossover frequency in *hcr1-1* after transformation with *PPX1* or empty vector constructs. **g**, As in **a**, but showing *420* crossover frequency in *hcr1-1, hcr1-2* and *hcr1-1/hcr1-2* F_1 hybrids. **h**, *420* crossover frequency in the *hcr1-2, ppx2* and *pp4r2* mutants. In **a**, **f**–**h**, mean cM values are indicated by red dots and horizontal lines.

PPX1 and *PPX2* transcript levels from meiotic stage floral buds in meiMIGS-transformed plants and observed a significant reduction of both genes in all tested lines, compared to wild type (Welch's *t*-test, all $P < 1.51 \times 10^{-9}$) (Extended Data Fig. 5). Cross-silencing of *PPX1* and *PPX2* by the meiMIGS constructs is expected, as these genes share 86.6% nucleotide identity. The constructs were transformed into *420*/++ plants and we observed a significant increase in crossover frequency compared to wild type (Welch's *t*-test, all

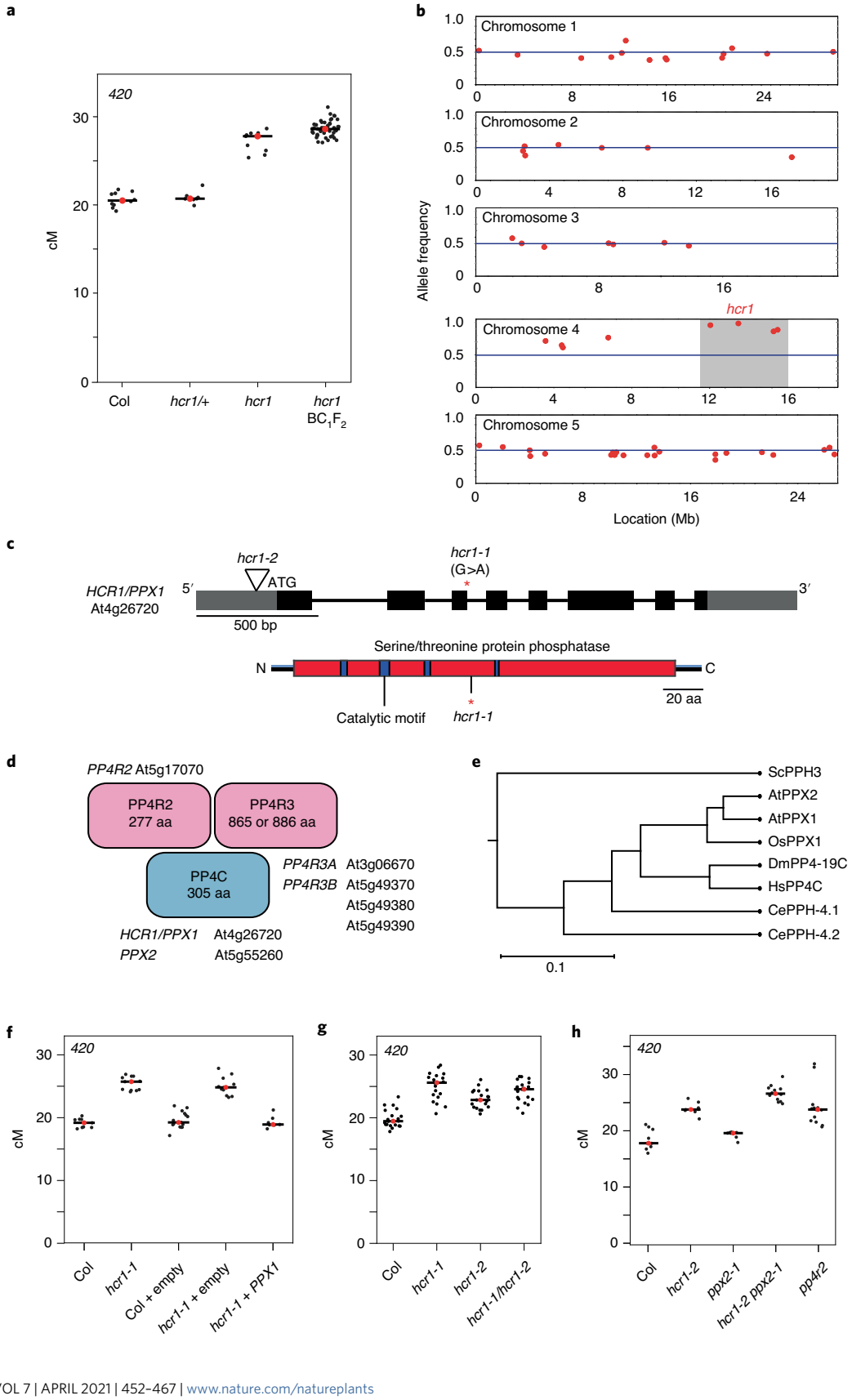

$P < 1.01 \times 10^{-4}$) (Fig. 3b and Supplementary Table 8). We correlated relative expression of *PPX1* and *PPX2* in these backgrounds with *420* crossover frequency and observed a significant negative correlation in both cases (*PPX1* $r = -0.76$, $P = 6.73 \times 10^{-5}$; *PPX2* $r = -0.64$ $P = 1.81 \times 10^{-3}$) (Fig. 3b,c and Extended Data Fig. 5). Together, these data demonstrate quantitative increases in crossover frequency that correlate with the degree of *PPX1* and *PPX2* silencing.

Euchromatic crossovers increase and the strength of interference decreases in *hcr1* and *meiMIGS-PPX1-PPX2*. To investigate the effect of *hcr1* and *meiMIGS-PPX1-PPX2* on crossover frequency in other genomic regions, we crossed these lines with additional FTL/CTL recombination reporters[29–31] (Fig. 3d) expressing fluorescent proteins using either seed (Fig. 3e,f), or pollen promoters (Fig. 3g). Plants carrying seed-based CTL reporters were self-fertilized and measure both male and female meiosis (Fig. 3e,f). We observed that distal FTL intervals *CTL1.17, CTL1.26*, *CTL3.15* and *CTL5.4* showed significantly higher crossover frequency in *hcr1-1*, compared to wild type (Welch's *t*-test, all $P < 1.08 \times 10^{-4}$) (Fig. 3e and Supplementary Table 9). By contrast, the centromere-spanning interval *CTL5.11* was not significantly different in *hcr1-1* (Fig. 3e and Supplementary Table 9). The same patterns were confirmed using *meiMIGS-PPX1-PPX2*, which showed significant crossover increases in the distal and interstitial FTL intervals *CTL1.13, CTL1.22, CTL2.2, CTL2.7, CTL4.7, CTL5.1* and *CTL5.13*, compared with wild type (Welch's *t*-test, all $P < 1.71 \times 10^{-3}$), whereas the centromeric interval *CTL5.5* were not significantly different (Fig. 3f and Supplementary Table 10).

We crossed *meiMIGS-PPX1-PPX2* with pollen-based FTL intervals, which are combined with the *quartet1* mutation[31] (Fig. 3d,g,h and Supplementary Tables 11 and 12). This assay measures crossover frequency and interference specifically in male meiosis[31]. For analysis, we used a deep learning pipeline DeepTetrad, which enables high-throughput analysis of fluorescent tetrads[54]. We tested four three-colour FTL intervals located in distal chromosome regions: *I1bc*, *I1fg*, *I3bc* and *I5ab*. All intervals, except the relatively narrow *I1g*, showed significant crossover increases in *meiMIGS-PPX1-PPX2* compared with wild type (Welch's *t*-test, all $P < 7.28 \times 10^{-3}$) (Fig. 3g, Extended Data Fig. 6 and Supplementary Table 11). We also tested the centromere-spanning FTL *CEN3*, which significantly decreased in *meiMIGS-PPX1-PPX2* (Welch's *t*-test, $P = 5.05 \times 10^{-3}$) (Fig. 3g and Supplementary Table 12). Across all FTL data, we correlated the proximity of each interval midpoint to the centromere, with the change in crossover frequency that occurred in *hcr1-1* or *meiMIGS-PPX1-PPX2* relative to wild type (Fig. 3i and Supplementary Tables 9–12). This analysis revealed a significant negative correlation ($r = -0.709$, $P = 1.48 \times 10^{-4}$) between the crossover increase and proximity to the centromere (Fig. 3i). These results show that the distal chromosome regions significantly increase crossovers in *hcr1* and *meiMIGS-PPX1-PPX2* when measured in male meiosis alone, or in both male and female meiosis. To specifically compare male and female recombination, we backcrossed wild type, *hcr1* and *meiMIGS-PPX1-PPX2* plants that were *420*/++ hemizygous, as either male or female parents. The *420* interval is heterochiasmic and shows significantly higher crossover frequency in males (24.23 cM), compared with females (10.98 cM) (Welch's *t*-test $P = 2.92 \times 10^{-6}$) (Fig. 3j and Supplementary Table 13). We observed that both *hcr1* and *meiMIGS-PPX1-PPX2* showed significant crossover increases in male (Welch's *t*-test $P = 6.25 \times 10^{-7}$ and 2.15×10^{-7}) and female (Welch's *t*-test $P = 2.81 \times 10^{-3}$ and 1.75×10^{-3}) meiosis, compared with wild type (Fig. 3j and Supplementary Table 13).

For three-colour, pollen-based FTL intervals we are able to measure crossovers in adjacent regions and thereby measure interference[31,54]. (Fig. 3h, Extended Data Fig. 6b and Supplementary Table 14). Crossover interference ratios (IFRs) are calculated using the genetic map distance in the test interval, with and without a crossover occurring in the adjacent interval. An IFR of 1 indicates an absence of interference[31,54]. We observed that *meiMIGS-PPX1-PPX2* causes an increase in crossover frequency, but a decrease in the strength of interference in FTLs *I1bc*, *I1fg*, *I3bc* and *I5ab* (Welch's *t*-test, all $P < 3.05 \times 10^{-3}$) (Fig. 3g,h and Supplementary Table 14). Therefore, a higher incidence of double crossovers in adjacent intervals occurs in *meiMIGS-PPX1-PPX2*, compared with wild type (Extended Data Fig. 6d). We repeated three-colour analysis using FTL intervals *I1bc* and *I3bc* in *hcr1-1* and again observed significantly increased crossover frequency and decreased crossover interference (higher IFR) (Welch's *t*-tests, $P = 2.7 \times 10^{-4}$ and $P = 8.1 \times 10^{-3}$, respectively) (Extended Data Fig. 6a–c and Supplementary Table 14).

Genome-wide mapping of crossovers in *meiMIGS-PPX1-PPX2*. Our FTL data indicate that the euchromatic chromosome arms undergo an increase in crossover frequency in *hcr1* and *meiMIGS-PPX1-PPX2*. Notably, these FTL experiments were performed in a Col/Col inbred background. Therefore, we sought to test the effect of *meiMIGS-PPX1-PPX2* on crossovers in a hybrid background (Fig. 4a). We crossed wild type (Col), or a *meiMIGS-PPX1-PPX2* transgenic line on the Col background carrying the *420* FTL, to Ler and generated Col/Ler F_1 hybrids (Fig. 4a and Supplementary Table 15). We measured *420* crossover frequency in wild type and *meiMIGS-PPX1-PPX2* Col/Ler F_1 hybrids and observed a significant increase in *meiMIGS-PPX1-PPX2* (Welch's *t*-test, $P = 6.55 \times 10^{-11}$) (Fig. 4b and Supplementary Table 15). This demonstrates that *PPX1* and *PPX2* repress crossovers in both inbred and hybrid backgrounds.

We self-fertilized wild-type and *meiMIGS-PPX1-PPX2* Col/Ler F_1 plants and generated 144 wild-type and 192 *meiMIGS-PPX1-PPX2* F_2 plants, from which we extracted genomic DNA. This DNA was sequenced and data were analysed using the TIGER pipeline[8,55] to identify crossover locations in each wild-type and *meiMIGS-PPX1-PPX2* F_2 individual (Fig. 4a,c–f). Crossovers

Fig. 3 | Euchromatic crossover frequency increases and crossover interference decreases in *hcr1* and *meiMIGS-PPX1-PPX2*. **a**, *meiMIGS-PPX1*, *meiMIGS-PPX2* and *meiMIGS-PPX1-PPX2* constructs. **b**, *420* crossover frequency (cM) in wild type, *meiMIGS-PPX1*, *meiMIGS-PPX2* and *meiMIGS-PPX1-PPX2* T_1 and T_2 transgenic lines. **c**, Correlation between *420* cM and *PPX1/HCR1* and *PPX2* transcript levels in floral buds of wild-type and *meiMIGS-PPX1*, *meiMIGS-PPX2* and *meiMIGS-PPX1-PPX2* T_2 transgenic lines. The *y*-axis represents *420* cM and the *x*-axis indicates fold enrichment of *PPX1* (blue) and *PPX2* (red) transcript levels compared with *PPX1* and *PPX2* in wild type, analysed by quantitative PCR with reverse transcription (RT–qPCR). *DMC1* was used as a meiotic gene for normalization. Mean values of triplicate RT–qPCRs were used. Data points represent wild type (Col) (black circle), *meiMIGS-PPX1* (red and blue circles), *meiMIGS-PPX2* (red and blue triangles) and *meiMIGS-PPX1-PPX2* (red and blue squares). **d**, FTL T-DNA intervals throughout the *Arabidopsis* genome used to measure crossover frequency. Circles indicate *LAT52*-driven FTL transgenes and triangles indicate *NapA*-driven FTL transgenes. CEN, centromere. **e**, As **c**, but showing FTL crossover frequency in wild type (blue) and *hcr1-1* (red). Mean values are indicated by horizontal black lines. **f**, As **c**, but showing FTL crossover frequency in wild type (blue) and *meiMIGS-PPX1-PPX2* (red). **g**, As **c**, but showing pollen-based FTL crossover frequency in wild type (blue) and *meiMIGS-PPX1-PPX2* (red). **h**, Crossover interference ratio measured using FTL pollen tetrads in wild type (blue) compared with *meiMIGS-PPX1-PPX2* (red). **i**, Correlation between FTL cM change in *hcr1-1* or *meiMIGS-PPX1-PPX2* and the midpoint of the FTL interval analysed relative to the telomere (TEL) and centromere. **j**, *420* crossover frequency (cM) in male and female meiosis of wild type (blue), *hcr1-1* (red) and *meiMIGS-PPX1-PPX2* (orange).

were mapped to an average of 962 bp and 936 bp in wild-type and *meiMIGS-PPX1-PPX2* F_2 populations, respectively (Supplementary Table 15). We observed a significant increase in crossovers per F_2 plant, from 7.86 in wild type, to 8.57 in *meiMIGS-PPX1-PPX2* (Welch's *t*-test, $P = 7.7 \times 10^{-3}$) (Fig. 4c), increased crossover numbers on each chromosome in *meiMIGS-PPX1-PPX2* compared with wild type (Fig. 4d), and a positive correlation between crossover number and chromosome length (wild type $r = 0.986$, *meiMIGS-PPX1-PPX2* $r = 0.983$) (Fig. 4d and Supplementary Table 16).

We analysed the crossover landscape in wild type and *meiMIGS-PPX1-PPX2* (Fig. 4e,f). We averaged all chromosome arms along their telomere–centromere axes and plotted crossover frequency per F_2 in wild-type and *meiMIGS-PPX1-PPX2* plants (Fig. 4e,f). Wild type and *meiMIGS-PPX1-PPX2* show a U-shaped distribution of crossover frequency along the chromosomes, with high recombination in the distal sub-telomeres and pericentromeres (Fig. 4e,f). We observed that the first 60–70% of the chromosome arms from the telomeres showed increased crossovers

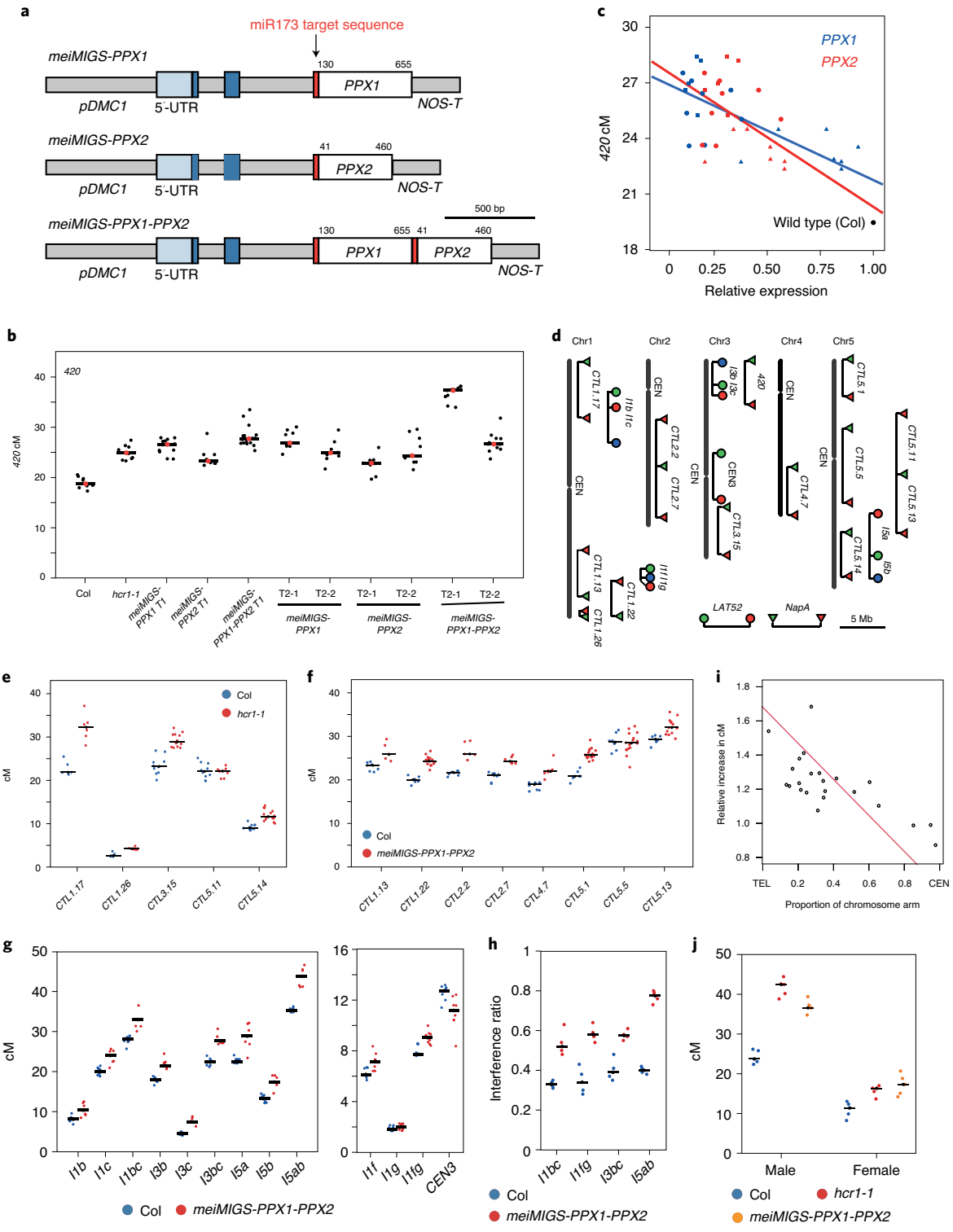

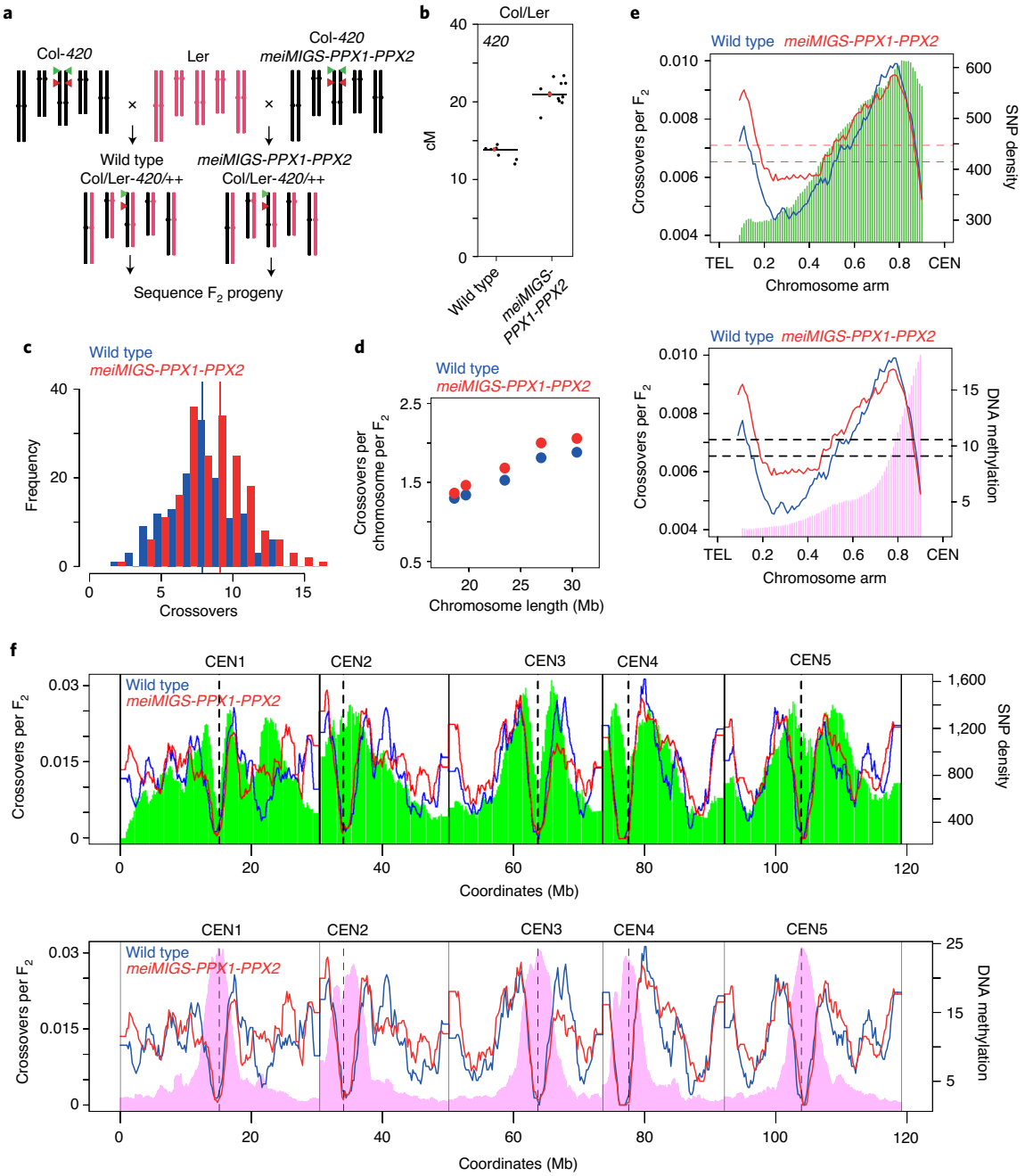

Fig. 4 | Genome-wide mapping of crossovers in *meiMIGS-PPX1-PPX2*. **a**, Schematic showing crossing of *meiMIGS-PPX1-PPX2* Col-*420* (black) and wild-type Col-*420* (black), to Ler (red) to generate F_2 populations for genotyping by sequencing. Green and red triangles indicate *420* T-DNAs on chromosome 3. **b**, *420* crossover frequency (cM) in wild type and *meiMIGS-PPX1-PPX2* Col/Ler F_1 hybrids. **c**, Histogram of crossover number per F_2 individual in wild-type (blue) Col/Ler and *meiMIGS-PPX1-PPX2* (red) populations. Vertical dashed lines indicate mean values. **d**, Crossovers per chromosome per F_2 compared with chromosome length in wild type (blue) and *meiMIGS-PPX1-PPX2* (red). **e**, Normalized crossover frequency plotted along chromosome arms orientated from telomere to centromere in wild-type (blue) and *meiMIGS-PPX1-PPX2* (red) F_2 populations. Mean values are indicated by horizontal dashed lines. Also plotted is Col/Ler SNP frequency (green, top) and DNA methylation (pink, bottom). **f**, As **e**, but without telomere–centromere scaling. Vertical solid lines indicate telomeres and vertical dashed lines indicate centromeres.

in *meiMIGS-PPX1-PPX2* compared with wild type, whereas the pericentromeres and centromeres showed a similar level of recombination (Fig. 4e,f), consistent with our previous FTL analysis (Fig. 3d–g,i). DNA methylation is highest in the centromeric region[33], where recombination is suppressed in both wild type and *meiMIGS-PPX1-PPX2* (Fig. 4e,f). We compared crossover frequency to Col/Ler single nucleotide polymorphism (SNP) frequency, which follows an ascending gradient from the telomeres to the centromeres (Fig. 4e,f). The distal regions of the chromosomes with lowest SNP density and lowest DNA methylation underwent the greatest crossover increase in *meiMIGS-PPX1-PPX2* compared with wild type (Fig. 4e,f). We analysed nucleosome occupancy (MNase-seq) and SPO11-1-oligonucleotides (a marker of meiotic DSBs) around crossover locations in wild type and *meiMIGS-PPX1-PPX2*, compared with the same number of randomly chosen locations[56,57]. We observed that crossovers in both

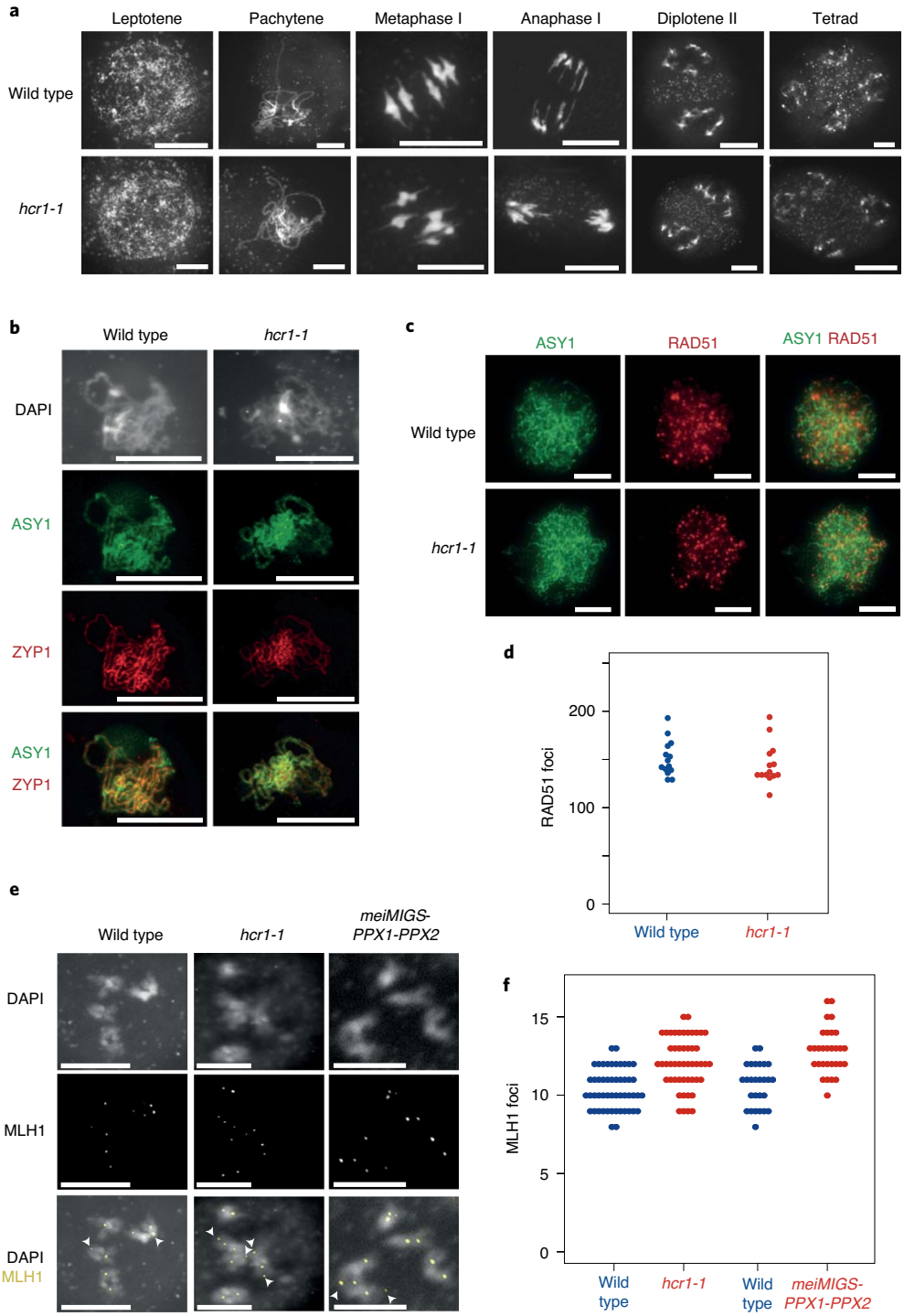

Fig. 5 | Meiotic MLH1 foci are elevated in *hcr1* whereas RAD51, ASY1 and ZYP1 immunostaining are unchanged. a, Representative images of male meiocytes spread and stained with DAPI in wild type (Col) and *hcr1-1*, at the indicated stages of meiosis. Scale bars, 10 µm. **b**, Representative images of ASY1 (green) and ZYP1 (red) immunostaining of wild type (Col-0) and *hcr1-1* male meiocytes at pachytene. Nuclei spreads were also stained with DAPI. Scale bars, 10 µm. **c**, Representative images of ASY1 (green) and RAD51 (red) co-immunostaining on wild-type (Col-0) and *hcr1-1* male meiocytes during early prophase I. Scale bars, 10 µm. **d**, Quantification of RAD51 foci number per cell in wild type and *hcr1-1*. **e**, Representative images of MLH1 immunostaining of male meiocytes at diakinesis stage in wild type, *hcr1-1* and *meiMIGS-PPX1-PPX2*. Cells were also DNA stained with DAPI. Arrows represent MLH1 foci at distal locations on the chromosomes. Scale bars, 10 µm. **f**, Quantification of MLH1 foci number per cell scored at diakinesis stage in wild type (blue), *hcr1-1* (red) and *meiMIGS-PPX1-PPX2* (red). All cytological experiments represent data collected from at least two biological replicates.

genotypes showed a similar depletion of nucleosome occupancy and enrichment of SPO11-1-oligonucleotides, compared to random positions (Extended Data Fig. 7). This indicates that while distal regions increase crossovers in *meiMIGS-PPX1-PPX2*, recombination retains a local bias for accessible DNA that experiences higher levels of DSB.

***hcr1* and *meiMIGS-PPX1-PPX2* show elevated class I MLH1 foci at diakinesis stage.** We used cytological analysis to analyse meiosis in *hcr1-1* compared with wild type. We spread wild-type and *hcr1-1* male meiocytes and stained chromosomes using 4′,6-diamidino-2-phenylindole (DAPI) (Fig. 5a). We observed normal chromosome morphology during prophase I (leptotene and pachytene) in *hcr1-1*, normal bivalent morphology at metaphase I and chromosome segregation during anaphase I and meiosis II (Fig. 5a). This is consistent with *hcr1-1* showing no difference in fertility compared with wild type (Supplementary Table 16). To investigate formation of the chromosome axis and homologue synapsis, we immunostained wild-type and *hcr1-1* meiocytes for the HORMA domain protein ASY1 and the synaptonemal complex protein ZYP1 during prophase I (Fig. 5b). Wild type and *hcr1-1* showed normal homologue synapsis and immunostaining of ASY1 and ZYP1 (Fig. 5b).

We immunostained meiocytes in early prophase I for ASY1 and the DSB marker RAD51 and observed no significant difference in RAD51 foci number between wild type and *hcr1-1* (Fig. 5c,d and Supplementary Table 18) (Wilcoxon *t*-test, $P=0.32$). This is consistent with normal levels of meiotic DSBs forming in *hcr1* relative to wild type. Finally, we immunostained for the MLH1 class I protein at diakinesis stage on DAPI-stained male meiocyte spreads (Fig. 5e,f and Supplementary Table 19). Quantification of MLH1 foci numbers per nucleus showed a significant increase in *hcr1-1* (mean = 12.1 foci), compared with wild type (mean = 10.4 foci) (Wilcoxon test, $P=5.3\times10^{-7}$) (Fig. 5e,f and Supplementary Table 19). We also measured MLH1 foci in wild type (Col) and *meiMIGS-PPX1-PPX2*, using the same transgenic line as for genotyping by sequencing. We observed that *meiMIGS-PPX1-PPX2* showed significantly higher numbers of MLH1 foci (mean = 12.8), compared with wild type (mean = 10.7) (Wilcoxon test $P=2.5\times10^{-6}$) (Supplementary Table 20). Together, this is consistent with the increases in crossovers observed in *hcr1* and *meiMIGS-PPX1-PPX2* being mediated mainly via the class I repair pathway.

HCR1 interacts with the class I crossover pathway proteins HEI10, PTD, MSH5 and MLH1. Since we observed elevated MLH1 foci in *hcr1* and *meiMIGS-PPX1-PPX2* (Fig. 5e,f), we sought to investigate genetic interactions with the class I and class II repair pathways. Class I pathway mutants, for example *zip4*, have low fertility due to reduced crossovers, unbalanced chromosome segregation and aneuploid gametes[14] (Fig. 5a). Fertility of class I mutants can be restored by mutations that block non-crossover formation and increase class II crossovers, for example *fancm*[37]. We generated *zip4 hcr1* double mutants and observed that fertility was not restored (Fig. 6a). We performed meiotic chromosome spreads and counted chiasma, bivalents and univalents in wild type (Col), *zip4* and *zip4 hcr1* (Supplementary Table 21). We observed that *zip4* and *zip4 hcr1* showed strongly reduced bivalents (*zip4* mean = 0.8, *zip4 hcr1* mean = 1.3), compared with wild type (mean = 5) (Wilcoxon test, Col versus *zip4* $P=5.22\times10^{-12}$, Col versus *zip4 hcr1* $P=1.43\times10^{-11}$). The bivalent counts for *zip4* and *zip4 hcr1* were not significantly different from one another (Wilcoxon test $P=0.11$). This is also consistent with a major effect of *hcr1* on the class I pathway. We also generated *hcr1 fancm* double mutants carrying the *420* FTL interval, and observed an additive increase in genetic distance in the double mutant compared to *hcr1* and *fancm* single mutants (Welch's *t*-tests, $P=2.7\times10^{-11}$ and $P=6.77\times10^{-6}$, respectively) (Fig. 6b and Supplementary Table 20). The *hcr1 fancm zip4* triple mutant exhibited a *420* crossover frequency lower than that of *hcr1 fancm*, but higher than that of *fancm zip4* (Welch's *t*-test, $P=5.60\times10^{-4}$ and $P=9.93\times10^{-4}$, respectively) (Fig. 6b and Supplementary Table 22). This suggests that *hcr1* may also increase the number of class II crossovers, at least in a *fancm zip4* mutant background (Fig. 6b and Supplementary Table 22).

We investigated whether HCR1 physically interacts with known components of the meiotic recombination pathways. We cloned HCR1/PPX1 into Y2H AD and BD vectors and tested interactions with class I proteins, as well as the PP4 regulatory subunits PP4R2L and PP4R3A (Fig. 6c,d, Extended Data Fig. 8 and Supplementary Table 23). As expected[28], HCR1 interacted strongly with the PP4 regulatory subunits PP4R2L and PP4R3A (Fig. 6c and Supplementary Table 23). Of the tested class I combinations, we observed strong Y2H interactions between HCR1 and HEI10, MSH5 and PTD (Fig. 6c,d). We also detected weaker interactions between HCR1 and the class I pathway proteins MER3, ZIP4, SHOC1 and MLH1 (Extended Data Fig. 8d and Supplementary Table 22). Within the class I pathway we observed strong interactions between HEI10, HEIP1 and MSH5, and between SHOC1 and PTD (Extended Data Fig. 8a,b), consistent with data in rice and *Arabidopsis*[12,58,59]. We additionally tested a wider set of 13 meiotic proteins that included the synaptonemal complex protein ZYP1a, DNA repair factors (DMC1, RAD51 and RPA1A), DSB proteins (PRD1, PRD2, PRD3, SPO11-1 and MTOPVIB) and meiotic chromosome axis proteins (ASY1, ASY3, SWI1 and REC8). Using serial dilutions, we observed that HCR1 shows strong interactions with REC8, SPO11-1, PRD1, RPA1A, MTOPVIB and PRD2 and weaker interactions with ASY1, RAD51, DMC1, ZYP1a and CDKA;1 (Fig. 6c,d and Extended Data Fig. 8a,b). Thus, although HCR1 represses the class I crossover pathway, it may have a more widespread role regulating protein phosphorylation during *Arabidopsis* meiosis.

The human PP4 complex targets multiple proteins by recognizing a short motif (FxxP) via the PP4R3 Ena/Vasp homology 1 (EVH1) domain[60]. To explore whether a similar mechanism is relevant in *Arabidopsis* we performed Y2H experiments using the *Arabidopsis* PP4R3A (At3g06670) EVH1 domain (residues 1–166) (Extended Data Fig. 9). The PP4R3A EVH1 domain interacts with 14 of 15 proteins observed as HCR1 interactors (Extended Data Fig. 9). Additionally, PP4R3A showed Y2H interactions with PRD3 and SWI1 (Extended Data Fig. 9). These data are consistent with HCR1/PPX1 and PP4R3A PP4 subunits interacting with a diverse set of proteins that regulate meiotic chromosomes and recombination, including class I factors.

We sought to further test protein–protein interactions between HCR1 and class I proteins in planta using transient transfection and co-localization studies in *Arabidopsis* protoplasts (Fig. 6e). As reported[51], expression of a HCR1–cyan fluorescent protein (CFP)

Fig. 6 | HCR1 genetically and physically interacts with the class I crossover pathway. a, Left: representative siliques from wild-type, *hcr1-1*, *zip4* and *hcr1-1 zip4* plants. Right: representative metaphase I chromosome spreads stained with DAPI from wild type (Col), *zip4* and *zip4 hcr1*. Images representative of three biological replicates. Scale bars, 10 µm. **b**, *420* crossover frequency (cM) in wild type, *hcr1-1*, *fancm*, *fancm zip4*, *hcr1-1 fancm* and *hcr1-1 fancm zip4*. Mean values are indicated by red dots and horizontal lines. **c**, Y2H assays showing interactions of HCR1 with PP4R2 and PP4R3. Yeast co-transformants were grown until optical density at 600 nm of 1, diluted 10-, 100- and 1,000-fold, spotted on synthetic dropout media (SD) deficient in leucine and tryptophan (−LT) or deficient in leucine, tryptophan, histidine and adenine (−LTHA) and grown for 3 to 7 d. **d**, As **c**, but showing interactions of HCR1 with HEI10, PTD and MSH5, and weaker interactions with SHOC1, MER3, ZIP4, MLH1, HEIP1 and ZYP1a. Yeast transformants were grown on SD (−LTHA) for 3, 5 or 7 d. **e**, Co-localization of fluorescent protein fusions with HCR1 and HEI10, PTD, MSH5 and MLH1 in *Arabidopsis* protoplasts. Scale bars, 20 µm. Experiments were repeated at least three times. **f**, Co-immunoprecipitation analyses of HCR1 and HEI10, PTD, MSH5 and MLH1. IB, immunoblot; IP, immunoprecipitation. Experiments were repeated at least three times.

fusion protein showed nuclear localization (Fig. 6e). We co-expressed PPX1–CFP with PTD–yellow fluorescent protein (YFP), HEI10–YFP, MSH5–YFP and MLH1–YFP fusion proteins and observed nuclear co-localization in all cases (Fig. 6e). We confirmed physical association of PPX1 using co-immunoprecipitation following transient expression in *Arabidopsis* protoplasts of PPX1–Myc,

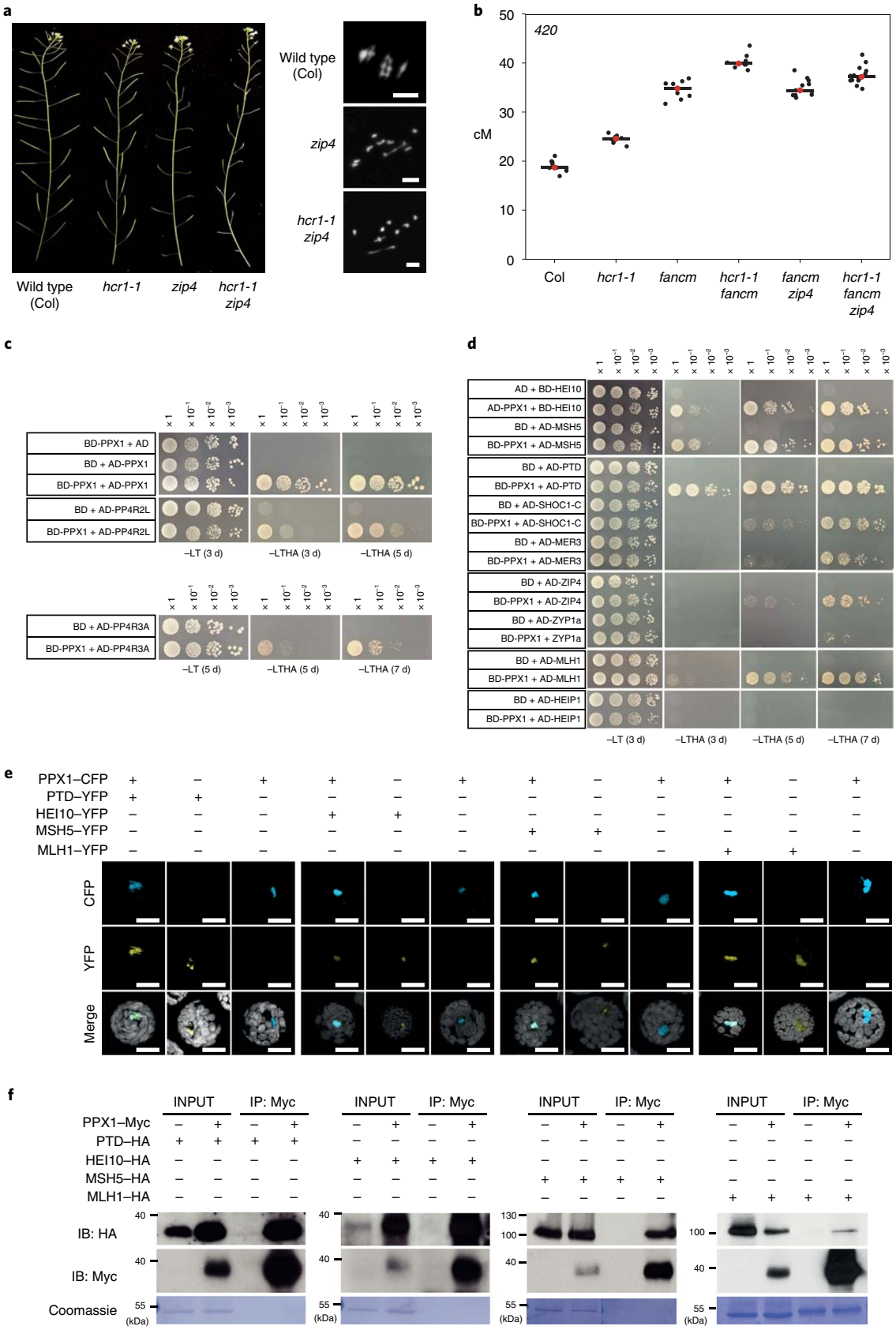

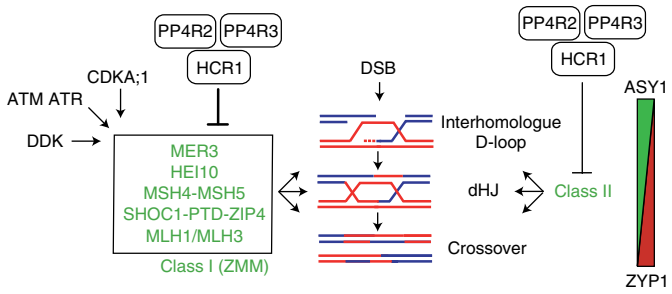

Fig. 7 | HCR1/PPX1–PP4 control of meiotic crossover recombination in *Arabidopsis*. During meiosis, recombination is initiated by DNA DSBs that can be resected to form ssDNA. Centre: a resected ssDNA end (blue) from one homologue has invaded the second homologue (red), to form an interhomologue displacement loop (D-loop). A subset of interhomologue D-loops are further processed to form double Holliday junctions (dHJs), which may be resolved into a crossover. The class I (also known as ZMM) pathway proteins (green) act at multiple steps in the formation and stabilization of interhomologue D-loops and dHJs and their resolution into interfering crossovers. The activity of the class I pathway has been shown to be promoted by independent kinase pathways, including CDK, DDK and Mec1/Tel1 (ATM/ATR). We propose that HCR1 acts with PP4R2 and PP4R3 in PP4 phosphatase complexes that antagonize one or more of the pro-recombination kinase pathways on class I targets and thereby restrict the number of interfering crossovers that form per meiosis. The class II pathway contributes to about 10% of crossovers in wild type. Our data also indicate a minor role for repression of the class II pathway by HCR1. Right: a diagram indicating that during progression of meiotic recombination, the abundance of axis protein ASY1 (green) is depleted, as the synaptonemal complex protein ZYP1 (red) increases.

together with PTD–haemagglutinin (HA), HEI10–HA, MSH5–HA or MLH1–HA (Fig. 6f). In each case, these experiments confirmed that these proteins interact in planta (Fig. 6f).

As discussed, human PP4 complexes bind the consensus motif FXXP via the PP4R3A EVH1 domain[60] (Extended Data Figs. 9a,b and 10). Interestingly, 15 out of 18 PPX1 interactors, and 12 out of 16 PP4R3A EVH1 interactors, identified using Y2H assays contain at least one FXXP motif (Extended Data Figs. 9 and 10 and Supplementary Table 20). The PPX1 and PP4R3A interactors also possess multiple consensus sites used by CDK, DDK and ATM/ATR kinases (Extended Data Fig. 10c and Supplementary Table 20). We searched genome-wide for potential meiotic PP4 substrates according to the criteria of: (1) FXXP motifs ($n = 13{,}803$), (2) predicted nuclear location ($n = 10{,}595$) and (3) meiocyte-specific expression[34,60] ($n = 4{,}528$). This search identified 1,367 candidate targets for the PP4 complex during meiosis (Extended Data Fig. 10d). Of these proteins, 1,315 (96.2%) have at least one phosphorylation consensus site (Extended Data Fig. 10e). Furthermore, 15 out of 18 PPX1 Y2H interactors, 12 out of 16 PP4R3A EVH1 Y2H interactors and 49 out of 84 known meiotic proteins were included in this list of candidate PP4 substrates (Extended Data Fig. 10e and Supplementary Table 23). The proportion of candidate PP4 substrates (1,367) with at least one phosphorylation site is significantly higher than the random expectation (compared with numbers of phosphorylation sites in 1,000 random sets of 1,367 proteins, Z-test $P = 7.02 \times 10^{-31}$) (Extended Data Fig. 10f). The 1,367 predicted meiotic PP4 substrates are also significantly enriched in Gene Ontology (GO) terms for DNA repair, DNA recombination, chromatin organization and meiosis I cell cycle (Extended Data Fig. 10g). Together, these data indicate the wide potential for PP4 regulation of meiosis and recombination in *Arabidopsis*.

Discussion

We identified the HCR1/PPX1 phosphatase as a repressor of crossover frequency in *Arabidopsis*. We provide genetic, cytological and protein–protein-interaction data that a major target of HCR1/PPX1 is the class I crossover pathway, and that it has a minor role repressing class II crossovers (Fig. 7). Our protein-interaction data indicate that HEI10, PTD, MSH5 and MLH1 are probably direct targets for HCR1/PPX1–PP4 phosphatase activity within the class I pathway. However, we also observed that HCR1/PPX1 and PP4R3A interact in a Y2H assay with components of the chromosome axis (ASY1, ASY3, REC8 and SWI1), DSB proteins (SPO11-1, MTOPVIB, PRD1 and PRD2) and recombinases (RPA1A, RAD51 and DMC1), consistent with a broader regulatory role during meiosis.

In the absence of HCR1/PPX1, we propose that the action of pro-recombination kinases on the class I pathway promotes stabilization of interhomologue strand invasion and crossover formation (Fig. 7). The crossover increases observed in *hcr1* and *meiMIGS-PPX1-PPX2* were most pronounced in the distal chromosome ends. Notably, distal crossover increases are characteristic of situations with elevated class I activity in *Arabidopsis*, including male meiosis, *HEI10* and *CDKA;1*[36,61,62], although distal increases are also observed in mutants that increase class II crossovers (for example, *recq4a recq4b*)[9,16,61]. The causes of distal biases in crossover formation in these backgrounds remain incompletely understood. Chromatin may be an important influence, as meiotic DSBs are elevated in gene-associated nucleosome-free regions, and there are positive associations with euchromatic chromatin marks, including H3K4me3 and H2A.Z[35,57,63,64]. By contrast, heterochromatic modifications including H3K9me2 and dense DNA methylation are associated with crossover suppression[33,65]. Additionally, class I crossovers are subject to interference, which inhibits formation of adjacent crossovers in a distance-dependent manner[11]. A complete understanding of the crossover landscape in *hcr1* will require further investigation of how chromatin, chromosome structure and interference co-operate spatially and temporally during meiosis.

Within the class I pathway, HEI10 belongs to a family of conserved ubiquitin or SUMO E3 ligases that promote interfering crossover formation in diverse eukaryotes[2,13]. In *Arabidopsis*, HEI10 is a dosage-sensitive promoter of class I crossover repair[16,36]. HEI10 shows a dynamic localization pattern along plant meiotic chromosomes, initially showing numerous foci along the axis, which become restricted to a small number of foci that overlap MLH1 foci during late prophase I[12,66,67]. In budding yeast, the HEI10 orthologue Zip3 is phosphorylated in a DSB-dependent manner by Mec1 (ATR), which is antagonized by PPH3[22]. This is of particular interest as PPH3 is a HCR1/PPX1 orthologue, indicating that repression of the class I pathway by PP4 phosphatases may be conserved between plants and fungi.

In mice, orthologues of HEI10 (for example, RNF212) act to regulate association of the MutSy Msh4–Msh5 heterodimer with meiotic chromosomes[68,69]. Msh4–Msh5 heterodimers are capable of forming sliding clamps on DNA in vitro and associate with recombination foci along meiotic chromosomes in vivo[70,71]. MutSy is proposed to bind nascent joint molecules and protect them from dissolution by anti-recombinases, including Sgs1–Top3–Rmi1 in budding yeast[70,72,73]. MutSy can also directly or indirectly recruit the MutLy (Mlh1–Mlh3) endonuclease heterodimer to promote crossover resolution[74–76]. Budding yeast Msh4 was recently identified as an intrinsically unstable protein that is degraded by the proteasome via an N-terminal degron[23]. Phosphorylation of the degron by the cell cycle kinase Cdc7–Dbf4 (DDK) inhibits Msh4 degradation and thereby promotes crossover repair[23]. As *Arabidopsis* HCR1/PPX1 physically interacts with MSH5 and MLH1 this may promote MutSy and MutLy dephosphorylation and thereby repress class I crossover repair.

We observed physical interaction between HCR1/PPX1 and PTD, which is the partner protein of SHOC1, which together form

a XPF–ERCC1-related complex[59,77–79]. Orthologues of the SHOC1–PTD complex include budding yeast Zip2–Spo16, which binds branched DNA molecules in vitro, lacks endonucleolytic activity and acts with Zip4 to promote crossover formation[79,80]. However, phosphorylation of Zip2–Spo16–Zip4 has been not reported in budding yeast or other organisms. Since *Arabidopsis* PTD interacts with HCR1 and PP4R3A EVH1 and contains consensus phosphorylation sites, it is possible that plant SHOC1–PTD–ZIP4 complexes may be regulated by phosphorylation.

It is also possible that HCR1/PPX1 may regulate phosphorylation of the DSB machinery, or components of the meiotic chromosome axis, as observed in *Caenorhabditis elegans*[81]. Furthermore, orthologues of ASY1 (Hop1), REC8 (Rec8) and ZYP1 (Zip1) proteins in budding yeast are known to be regulated via phosphorylation[24,25]. Hence, it is possible that *Arabidopsis* ASY1, REC8 and ZYP1 may be dephosphorylated by PP4. However, we did not observe significant changes to RAD51 foci or ASY1 and ZYP1 immunostaining during meiosis in *hcr1* at the cytological level.

We consider three pro-recombination kinase pathways as candidates for HCR1/PPX1–PP4 antagonism (Fig. 7). First, CDK–cyclin complexes are drivers of cell cycle progression, including during meiosis and are known to regulate recombination[18,62,82]. Second, Dbf4-dependent kinase (DDK) (Cdc7–Ddf4) has a prominent role in the initiation of DNA replication, and also in regulation of recombination and kinetochore behaviour during meiosis[83–88]. Third, the ATM/ATR phosphatidylinositol 3-kinase-related kinases are activated by DSBs and regulate meiotic DSB number and distribution in yeast and mammals[19–21]. Together these kinase pathways play complex and interacting roles in the promotion of crossovers during meiosis[89].

In *Arabidopsis*, CDKA;1 (the homologue of human Cdk1 and Cdk2) has a role in promoting class I crossovers[62,90]. Hence, HCR1/PPX1 may remove phosphorylation from CDKA;1 targets within the class I pathway and thereby limit crossovers (Fig. 7). Interestingly, mutation of CDK consensus motifs (S/T-P) in budding yeast Zip3 had no effect on phosphorylation, whereas mutation of Tel1/Mec1 sites (S/T-Q) did[22]. As noted earlier, Zip3 phosphorylation has been shown to be regulated by PP4[22], meaning that HCR1 may regulate HEI10 phosphorylation in an analogous manner in *Arabidopsis* (Fig. 7). Indeed, it has been shown that many targets of Mec1 phosphorylation, including Zip1, are also PP4 substrates in budding yeast[48]. In *Arabidopsis*, ATM and ATR are redundantly required for DSB repair[91]. The *atm* single mutant is partially sterile with increased meiotic DSBs, chromosomal fragmentation and moderately increased class I crossovers[92,93]. In budding yeast, DDK is responsible for Msh4 degron phosphorylation and stabilization[23]. Thus, it is possible that HCR1 could dephosphorylate MutSy and thereby promote its destabilization and repress crossovers (Fig. 7). However, the meiotic function of DDK kinases in plants is currently unknown.

Studies in diverse systems and contexts have identified PP4 phosphatase complexes as key regulators of DNA repair and recombination. For example, the DNA-damage response involves kinase regulation, which is balanced with antagonizing phosphatases[41]. Defined roles for PP4 complexes include: (1) dephosphorylation of γ-H2AX during recovery from DNA-damage checkpoints in *Drosophila*, budding yeast and human[42–45], (2) prevention of Rad53 hyperphosphorylation during DSB repair and promoting DNA end resection in budding yeast[94], (3) dephosphorylating RPA2 to promote DNA repair via homologous recombination[27], (4) promoting non-homologous end joining-mediated DSB repair, which occurs partially via KRAB-associated protein1 (KAP1)[47], (5) regulation of Mec1 during DSB repair and at sites of replication fork collapse[26], and (6) regulating Zip1 phosphorylation during meiosis to control homology-independent centromere pairing[48]. Our work identifies PPX1–PP4 phosphatase complexes as repressing the class I crossover pathway during *Arabidopsis* meiosis. We propose that PP4 complexes may generally act in opposition to pro-recombination kinases to regulate meiotic crossovers in eukaryotes.

Methods

Plant materials. *Arabidopsis thaliana* plants were grown under controlled conditions of 22 °C, 50–60% humidity and 16:8 h light:dark cycles. Seeds were incubated at 4 °C in the dark for 3–4 d to stratify germination. Seed-expressed FTL/CTL and pollen-expressed FTL lines were used[29,30]. T-DNA insertion lines in *ppx1* (GK_651B07), *ppx2* (GK_488H09), *pp4r2* (SALK_093051), *zip4-2*[95] (SALK_068052) and the *fancm-1* EMS mutant[37] were provided by Nottingham *Arabidopsis* Stock Centre. Genotyping of *hcr2-1* was performed by PCR amplification using oligonucleotides ppx1-F and ppx1-R for wild type, and ppx1-F and GABI_LB for the T-DNA allele. Genotyping of *ppx2-1* was carried out by PCR amplification using primers ppx2-F and ppx2-R for wild type, and ppx2-R and GABI_LB for the T-DNA allele. Genotyping of *pp4r2* was performed by PCR amplification using oligonucleotides pp4r2-F and pp4r2-R for wild type, and pp4r2-R and LBb1.3 for the T-DNA allele. Genotyping of *hcr1-1* was performed by PCR amplification using hcr1-F and hcr1-R dCAPs markers, followed by FokI restriction endonuclease digestion. *zip4-2* and *fancm-1* genotyping was performed as previously described[33]. Genotyping oligonucleotide sequences can be found in Supplementary Table 24.

Ethyl-methyl sulfonate mutagenesis of *A. thaliana* seed. Approximately 10,000 seeds from *420 GR/++* hemizygote plants were obtained by crossing *420* (*GR/GR*) homozyotes to wild type (Col-0). These seed were soaked in 40 ml of 100 mM phosphate buffer (pH 7.5) in a 50 ml tube for 1 h. Seeds were washed with fresh 100 mM phosphate buffer and then treated with 0.3% (v/v) ethyl-methyl sulfonate and incubated for 12 h at room temperature. Seeds treated with ethyl-methyl sulfonate were washed ten times with distilled water and immediately sown on soil. From these seeds, ~7,000 M_1 plants were germinated and grown. The seeds from 12 independent M_1 plants were combined to generate ~600 M_2 pools. From each M_2 pool, ~150 seeds were pre-selected as *420/++* hemizygotes on the basis of red and green fluorescence, grown and self-fertilized. The resulting seeds were analysed for *420* crossover frequency.

Measurement of crossover frequency and interference using fluorescent seed and pollen. Crossover frequency was measured by analysing counts of fluorescent and non-fluorescent seeds from *FTL/++* hemizygote plants using a CellProfiler image analysis pipeline[96,97]. CellProfiler enables the quantification of the numbers of green-only fluorescent seeds (N_{Green}), red-only fluorescent seeds (N_{Red}) and total seeds (N_{Total}). Crossover frequency (cM) is calculated using the formula[30,32]: $cM = 100 \times (1 - [1 - 2(N_{Green} + N_{Red})/N_{Total}]^{1/2})$. To test whether crossover frequency was significantly different between genotypes, we used Welch's *t*-tests.

Pollen FTLs were generated on the *qrt-1* mutant background, where the four-pollen products of male meiosis are attached to one another[31]. FTLs express eYFP, dsRed or eCFP fluorescent proteins under the post-meiotic *LAT52* promoter. Pollen tetrad FTL-based measurement of crossover frequency and interference were carried out using DeepTetrad, as described[31,54]. DeepTetrad is a deep learning-based image analysis pipeline that recognizes pollen tetrad classes of two- or three-colour FTL intervals. The two-colour FTL interval *CEN3* produces parental ditype (PD), tetra type (*T*), and non-parental ditype (NPD) tetrads, and crossover frequency was calculated using the Perkin's equation:

$$\mathrm{cM} = \frac{0.5T + 3\mathrm{NPD}}{(\mathrm{PD} + T + \mathrm{NPD})} \times 100$$

Three-colour FTL intervals (*I1bc, I1fg, I2fg, I3bc* and *I5ab*) produce 12 tetrad classes: no recombination (*A*), single crossover interval 1 (*B*; SCO-i1), single crossover interval 2 (*C*; SCO-i2), two-strand double crossover (*D*; 2stDCO), three-strand double crossover a (*E*; 3st DCOa), three-strand double crossover b (*F*; 3st DCOb), four-strand double crossover (*G*; 4st DCO), non-parental ditype interval 1, non-crossover interval 2 (*H*; NPD-i1 NCO-i2), non-crossover interval 1, non-parental ditype interval 2 (*I*; NCO-i1 NPD-i2), non-parental ditype interval 1, single crossover interval 2 (*J*; NPD-i1 SCO-i2), single crossover interval 1, non-parental ditype interval 2 (*K*; SCO-i1 NPD-i2) and non-parental ditype interval 1, non-parental ditype interval 2 (*L*; NPD-i1 NPD-i2)[31]. Fluorescent tetrad states were identified using DeepTetrad and cM was calculated using the Perkin's equation.

Crossover interference ratio (IFR = σ) in two linked intervals, which is the ratio of the genetic map distance with an adjacent crossover χ_γ to the genetic map distance without an adjacent crossover χ_δ, was calculated by DeepTetrad using the formulae

$$\chi_\gamma = \frac{0.5T_\gamma + 3\mathrm{NPD}_\gamma}{\mathrm{PD}_\gamma + T_\gamma + \mathrm{NPD}_\gamma} = \frac{0.5(D+E+F+G+K)+3(J+L)}{(C+I)+(D+E+F+G+K)+(J+L)}$$

$$\chi_\delta = \frac{0.5T_\delta + 3\mathrm{NPD}_\delta}{\mathrm{PD}_\delta + T_\delta + \mathrm{NPD}_\delta} = \frac{0.5(B)+3(H)}{(A)+(B)+(H)}$$

$$\sigma = \frac{\chi_\gamma}{\chi_\delta}$$

Identification of candidate *hcr1-1* mutations using DNA sequencing and SHOREmap. Sixty *hcr1* BC_1F_2 individuals with high (>27 cM) *420* crossover frequency were identified and 5 mg of seeds from each BC_1F_2 individual were pooled. Sterilized seeds were germinated on 1/2 MS agar plates and bulk 7-day-old seedlings were collected. About 3 g of pooled seedlings was ground in liquid N_2 using a mortar and pestle. The leaf powder was transferred into a pre-chilled mortar with 40 ml of fresh nuclear isolation buffer (25 mM Tris-HCl, pH 7.5, 0.44 M sucrose, 10 mM $MgCl_2$, 0.5% Triton X-100, 10 mM β-mercaptoethanol, 2 mM spermine and EDTA-free protease inhibitor cocktail) and the contents were homogenized. The tissue lysate was kept on ice and incubated for 30 min with rocking. The filtered contents were centrifuged at 4 °C at 3,000*g* for 25 min. The supernatant was removed and the pellet was subjected to DNA extraction using cetyl trimethylammonium bromide (CTAB). CTAB-extracted and purified DNA was sheared to a size range 200–500 bp using a Bioruptor sonicator. One microgram of input DNA was diluted in 150 µl of TE buffer and sonicated for 22 min using high voltage with 30 s ON/OFF cycles. The sonicated DNA was concentrated in a 60 µl volume and DNA in the size range ~300–400 bp from a 2% agarose gel stained with 1× SYBR gold using a UV transilluminator. Fifty nanograms of purified DNA in 60 µl was used as input for library construction using an Illumina Truseq Nano DNA LT library prep kit. The *hcr1-1* BC_1F_2 library was sequenced using an Illumina Genome Analyser (100 bp paired) Hiseq 2000 instrument.

SHOREmap (v.3.0) was applied to align paired-end reads to the TAIR10 reference genome using the GenomeMapper tool[38]. Raw reads were trimmed according to quality values with a cut-off Phred score of +33 or +64, using the function SHORE import. SHORE function consensus was used to detect sequence variation between the *hcr1* BC_1F_2 and the TAIR10 reference assembly. SNPs with high-quality marker scores (>40), supported by at least 10 unique reads, were applied using SHOREmap backcross for analysis of allele frequency. Using SHOREmap annotate, we compared the TAIR10 gene annotation and obtained a list of EMS-derived mutations that included predicted effects on gene expression and function. Mutations were screened for those with (1) greater than 80% allele frequency, and (2) non-synonymous, splice site or premature stop codon changes in predicted genes. Additionally, candidate mutations were examined on the basis of their location within genes with predicted or known functions relevant to meiosis, protein location in the nucleus and known molecular functions provided in the The *Arabidopsis* Information Resource (TAIR) database.

Genetic complementation of *hcr1-1* by *PPX1*. A 4.5-kb genomic DNA fragment containing *HCR1*/*PPX1* was amplified by PCR using primers PPX1-F and PPX1-R (Supplementary Table 24). The PCR product was digested by *Pst*I and *Sma*I restriction enzymes and cloned into the binary vector pGREEN0029. The pGREEN0029-*PPX1* and empty vector constructs were electroporated into *Agrobacterium* strain GV3101-pSOUP and transformed into *Arabidopsis* plants by floral dipping[98]. T_1 plants were selected for kanamycin resistance and genotyped using primers designed from left and right borders of the *HCR1*/*PPX1* transgene (Supplementary Table 24).

Construction of PPX/PP4 phylogenetic tree. The neighbour-joining method was used to construct a PPX/PP4 phylogenetic tree. Amino acid sequences of AtPPX1 (NP_194402.1), AtPPX2 (NP_200337.1), OsPPX (XP_015612628), DmPp4-19C (NP_001285489), HsPPP4C (NP_001290432), Cepph-4.1 (NP_499603), Cepph-4.2 (NP_001022898) and ScPPH3 (AJV04101) were used for multiple sequence alignments.

Generation of *meiMIGS-PPX1*, *meiMIGS-PPX2* and *meiMIGS-PPX1-PPX2* transgenic plants. To generate meiosis-specific microRNA mediated gene silencing (*meiMIGS*) transgenic plants, 1.5 kb of genomic DNA including the *DMC1* promoter, 5′-UTR, two introns and the third exon were amplified by PCR from Col genomic DNA using primers DMC1-1p_1.5kb-Lv0-GGAG-F and DMC1-1p_1.5kb-Lv0-CATT-R (Supplementary Table 24). PCR products was cloned into the universal Level 0 (Lv0) vector (pAGM9121) using the Golden Gate cloning system. *PPX1* and *PPX2* cDNA regions were cloned into the Lv0 vector (pAGM9121) following amplification using forward primers that included the miR173 target sequence and reverse primers (Supplementary Table 21). *PPX1-PPX2* fusion cDNA was generated by overlap PCR and cloning into Lv0 vector pAGM9121. The *DMC1* promoter and *MIGS-PPX1/2/1-2* Lv0 vectors were assembled into Lv1 position 2 vector pICH47742 with the *NOPALINE SYNTHASE GENE* (*NOS*) terminator (pICH41421). Each Lv1 vector containing meiMIGS cassettes was assembled into a Level 2 (Lv2) binary vector (pAGM4723) with the antibiotic resistant gene *BAR* containing Lv vector (pICSL11017) and linker (pICH41744). The Lv2 binary vectors were electroporated into *Agrobacterium* strain GV3101-pSOUP and transformed into *Arabidopsis* by floral dipping.

Genotyping by sequencing of F_2 plants and crossover identification. Genomic DNA from wild type and *meiMIGS-PPX1-PPX2* Col/Ler F_2 individuals was extracted using CTAB to prepare sequencing libraries, as described[55]. DNA (150 ng) was fragmented using 0.3 units of dsDNA Shearase (Zymo Research) in a final volume of 15 µl. The digested DNA was end-repaired for 30 min at 20 °C in a reaction volume of 30 µl (3 units of T4 DNA polymerase (New England Biolabs), 10 units of T4 polynucleotide kinase (Thermo Fisher Scientific), 1.25 units of Klenow fragment (New England Biolabs) and 0.4 mM dNTPs). DNA fragments were cleaned using AMPure XP magnetic solid-phase reversible immobilization (SPRI) beads (Beckman-Coulter, A63881), as described[55]. DNA was A-tailed, and then ligated with barcoded Illumina adapters in a reaction volume of 20 µl, as described[55]. Eight DNA libraries were pooled, washed and eluted in 30 µl elution buffer (10 mM Tris-HCl, pH 8.0). The 30 µl mixture was combined in a tube containing 16 µl of AMPure XP magnetic SPRI beads (Beckman-Coulter). After 5 minutes of incubation at room temperature, the samples were placed in a magnetic rack for 2 minutes and the supernatant (42 µl) was transferred to a fresh tube and mixed with 0.23 volumes (9.5 µl) of SPRI beads. After 5 min of incubation at room temperature, the tubes were placed on a magnetic rack for 2 min. The supernatant was discarded, and the beads washed twice with 80% ethanol for 30 s. The beads were air-dried for 10 min and DNA was eluted in 20 µl of 10 mM Tris (pH 8.0). Twelve microlitres of the eluate was amplified using twelve cycles of PCR in a reaction volume of 50 µl using KAPA HiFi Hot-Start ReadyMix PCR kit (Kapabiosystems) and the reported DNA oligonucleotides[55]. The PCR products were then purified using SPRI beads and quantified using a Bioanalyzer. The 96 barcoded libraries were subjected to paired-end 150 bp sequencing using an Illumina HiSeqX instrument.

Immunocytological analysis of wild-type and *hcr1* meiocytes. Chromosome spreads of *Arabidopsis* pollen mother cells were prepared using fixed buds and stained with DAPI as described[99]. Pachytene cells were immunostained for ASY1 and ZYP1, and diakinesis cells were immunostained for MLH1, using fixed buds, as described[99,100]. Leptotene-stage meiocytes were immunostained for ASY1 and RAD51 using fresh buds, as described[101]. The following antibodies were used: ASY1 (rat, 1:200 or 1:500 dilution), ZYP1 (rabbit, 1:200 dilution), MLH1 (rabbit, 1:200 dilution) and RAD51 (rabbit, 1:300 dilution)[99,101,102]. Microscopy was performed using a DeltaVision personal DV microscope (Applied precision/GE Healthcare) equipped with a CCD Coolsnap HQ2 camera (Photometrics). Image capture was carried out using SoftWoRx software version 5.5 (Applied precision/GE Healthcare). For ASY1 and RAD51 co-immunostaining of leptotene-stage nuclei, individual cell images were acquired as *Z*-stacks of 10 optical sections of 0.2 µm each, and the maximum intensity projection for each cell was decided using ImageJ. Number of MLH1 foci per meiotic cell and RAD51 foci per cell associated with the axis protein ASY1 were manually scored. Wilcoxon tests were used to assess significant differences between wild type and *hcr1-1* MLH1 and RAD51 foci counts.

Y2H assays. For Y2H assays, the open reading frames of *Arabidopsis* genes were cloned into pGBKT7 BD and pGADT7 AD vectors (Clontech, 630490) using BamHI and StuI sites, using a Gibson assembly cloning system (NEB E2621L). Information on all oligonucleotides used for Y2H assays is presented in Supplementary Table 24. BD and AD vectors were co-transformed into *S. cerevisiae* strain AH109 and selected on synthetic dropout medium lacking leucine (−L) and tryptophan (−T). The colonies of yeast transformant cells were streaked onto both (−LT) and (−LTH (histidine) A (adenine)) synthetic media and grown for 3–5 d at 30 °C. The cells grown in synthetic medium (−LT) were grown until $OD_{600} = 1$ and diluted 10-, 100- and 1,000-fold in water and spotted on synthetic medium (−LTHA) for 3–7 d.

Transient expression of fusion proteins in *Arabidopsis* protoplasts for co-localization and co-immunoprecipitation analysis. Transient expression vectors in protoplasts were constructed using Golden Gate cloning. The full-length coding regions of *PPX1*/*HCR1* and meiotic genes were amplified by PCR from cDNA and cloned into Lv0 universal vector (pICH41331). For epitope and fluorescent protein tagging, Lv0 vectors with coding regions lacking a stop codon were assembled in the Lv1 transient expression vector (pICH47742), using the *35S* promoter vector (pICH51266), C-terminal vectors (YFP, CFP, Myc tag/pICSL50010 and HA tag/pICSL50009) and *NOS* terminator vector (pICH41421). Information on all oligonucleotides for protoplast transient expression is provided in Supplementary Table 24.

Plasmid DNA and mesophyll protoplasts were prepared as described[103]. Twenty-thousand protoplasts were transfected with 20 µg of total plasmid DNA and incubated for 6–12 h at room temperature. To detect co-localization of PPX1–CFP and meiotic protein–YFP, 20 µg of total plasmid DNA (a mixture of *PPX1-CFP* with *YFP* fusion constructs *HEI10-YFP, PTD-YFP* or *MSH5-YFP*) were co-transfected into 20×10^3 protoplasts and incubated at room temperature for 12 h. As a negative control, *PPX1-CFP* alone or *YFP* fusion plasmid alone were transfected. The fluorescence of transfected mesophyll protoplasts was detected using a confocal microscope (LSM 800, Zeiss).

For co-immunoprecipitation analysis, 40 µg of *PPX1*-Myc tag and meiotic gene-HA tag DNA plasmids were co-transfected into protoplasts, or individually transfected as a negative control. Total protein was extracted using extraction buffer (50 mM Tris-HCl pH 7.5, 100 mM NaCl, 5 mM EDTA, 1 mM dithiothreitol, protease inhibitor cocktail (Roche) and 1% Triton X-100). The extracted proteins were separated by SDS–PAGE using 8% polyacrylamide gels, transferred to a

nitrocellulose membrane and immunodetected with anti-HA (1:2,000 Roche 12013819001) or anti-Myc (1:2,000 Santa Cruz sc-9E10) antibodies. For co-immunoprecipitation analysis, transfected protoplasts were lysed with IP buffer (50 mM Tris-HCl pH 7.5, 100 mM NaCl, 1 mM EDTA, 0.5% Triton X-100, 10% glycerol and protease inhibitor cocktail). Lysates were incubated with 1 µg anti-Myc antibody for 12 h with rotation at 4 °C. Then, the protoplast lysate and antibody mixture were incubated with 50% protein G-coated agarose beads (Millipore 16-201), pre-cleared with IP buffer, for an additional 2 h. Protein-coated agarose beads were washed with IP buffer three times. Proteins were extracted using extraction buffer and analysed by western blotting using anti-HA antibodies.

Prediction of PP4 complex target proteins in *Arabidopsis*. To predict PP4 target proteins during meiosis, proteins containing the FXXP motif were identified by searching protein sequences from TAIR. Nuclear proteins were obtained from the TAIR10 GO cellular compartment annotation by selecting terms 'nucleus', 'other cellular components: host cell nucleus' and 'other cellular components: nucleus-vacuole junction'. We used a previous RNA-seq dataset, which identified genes that showed significantly higher expression in male meiocytes compared with leaf[34]. The meiotically expressed, nuclear proteins with FXXP motifs were further classified according to the presence of predicted phosphorylation consensus sites of CDK, DDK and ATM/ATR, predicted using GPS 5.0[104]. To test for significant enrichment of phosphorylation consensus motifs in the predicted PP4 target proteins, we generated random sets of the same number of genes which were analysed for predicted phosphosites. The observed phosphosite overlaps were compared with the random using a *Z*-test.

Reporting Summary. Further information on research design is available in the Nature Research Reporting Summary linked to this article.

Data availability

Genome sequencing data of F_2 plants can be found at the ArrayExpress repository hosted by the European Bioinformatics Institute under accessions E-MTAB-9621 and E-MTAB-10168. Source data are provided with this paper.

Received: 1 September 2020; Accepted: 25 February 2021;
Published online: 12 April 2021

References

1. Villeneuve, A. M. & Hillers, K. J. Whence meiosis? *Cell* **106**, 647–650 (2001).
2. Mercier, R., Mézard, C., Jenczewski, E., Macaisne, N. & Grelon, M. The molecular biology of meiosis in plants. *Annu. Rev. Plant Biol.* **66**, 297–327 (2015).
3. Grelon, M., Vezon, D., Gendrot, G. & Pelletier, G. AtSPO11-1 is necessary for efficient meiotic recombination in plants. *EMBO J.* **20**, 589–600 (2001).
4. Robert, T. et al. The TopoVIB-Like protein family is required for meiotic DNA double-strand break formation. *Science* **351**, 943–949 (2016).
5. Hartung, F. et al. The catalytically active tyrosine residues of both SPO11-1 and SPO11-2 are required for meiotic double-strand break induction in *Arabidopsis*. *Plant Cell* **19**, 3090–3099 (2007).
6. Hunter, N. Meiotic recombination: the essence of heredity. *Cold Spring Harb. Perspect. Biol.* **7**, a016618 (2015).
7. Ferdous, M. et al. Inter-homolog crossing-over and synapsis in *Arabidopsis* meiosis are dependent on the chromosome axis protein AtASY3. *PLoS Genet.* **8**, e1002507 (2012).
8. Rowan, B. A. et al. An ultra high-density *Arabidopsis thaliana* crossover map that refines the influences of structural variation and epigenetic features. *Genetics* **213**, 771–787 (2019).
9. Girard, C. et al. AAA-ATPase FIDGETIN-LIKE 1 and helicase FANCM antagonize meiotic crossovers by distinct mechanisms. *PLoS Genet.* **11**, e1005369 (2015).
10. Cifuentes, M., Rivard, M., Pereira, L., Chelysheva, L. & Mercier, R. Haploid meiosis in *Arabidopsis*: double-strand breaks are formed and repaired but without synapsis and crossovers. *PLoS ONE* **8**, e72431 (2013).
11. Berchowitz, L. E. & Copenhaver, G. P. Genetic interference: don't stand so close to me. *Curr. Genomics* **11**, 91–102 (2010).
12. Li, Y. et al. HEIP1 regulates crossover formation during meiosis in rice. *Proc. Natl Acad. Sci. USA* **115**, 10810–10815 (2018).
13. Pyatnitskaya, A., Borde, V. & De Muyt, A. Crossing and zipping: molecular duties of the ZMM proteins in meiosis. *Chromosoma* **128**, 181–198 (2019).
14. Mercier, R. et al. Two meiotic crossover classes cohabit in *Arabidopsis*: one is dependent on MER3,whereas the other one is not. *Curr. Biol.* **15**, 692–701 (2005).
15. Séguéla-Arnaud, M. et al. Multiple mechanisms limit meiotic crossovers: TOP3α and two BLM homologs antagonize crossovers in parallel to FANCM. *Proc. Natl Acad. Sci. USA* **112**, 4713–4718 (2015).
16. Serra, H. et al. Massive crossover elevation via combination of HEI10 and recq4a recq4b during *Arabidopsis* meiosis. *Proc. Natl Acad. Sci. USA* **115**, 2437–2442 (2018).
17. Marston, A. L. & Amon, A. Meiosis: cell-cycle controls shuffle and deal. *Nat. Rev. Mol. Cell Biol.* **5**, 983–997 (2004).
18. Yang, C. et al. The *Arabidopsis* Cdk1/Cdk2 homolog CDKA;1 controls chromosome axis assembly during plant meiosis. *EMBO J.* **39**, 1–19 (2020).
19. Lange, J. et al. The landscape of mouse meiotic double-strand break formation, processing, and repair. *Cell* **167**, 695–708 (2016).
20. Garcia, V., Gray, S., Allison, R. M., Cooper, T. J. & Neale, M. J. Tel1(ATM)-mediated interference suppresses clustered meiotic double-strand-break formation. *Nature* **520**, 114–118 (2015).
21. Lange, J. et al. ATM controls meiotic double-strand-break formation. *Nature* **479**, 237–240 (2011).
22. Serrentino, M.-E., Chaplais, E., Sommermeyer, V. & Borde, V. Differential association of the conserved SUMO ligase Zip3 with meiotic double-strand break sites reveals regional variations in the outcome of meiotic recombination. *PLoS Genet.* **9**, e1003416 (2013).
23. He, W. et al. Regulated proteolysis of MutSγ controls meiotic crossing over. *Mol. Cell* **78**, 168–183 (2020).
24. Carballo, J. A., Johnson, A. L., Sedgwick, S. G. & Cha, R. S. Phosphorylation of the axial element protein Hop1 by Mec1/Tel1 ensures meiotic interhomolog recombination. *Cell* **132**, 758–770 (2008).
25. Brar, G. A. et al. Rec8 phosphorylation and recombination promote the step-wise loss of cohesins in meiosis. *Nature* **441**, 532–536 (2006).
26. Hustedt, N. et al. Yeast PP4 interacts with ATR homolog Ddc2–Mec1 and regulates checkpoint signaling. *Mol. Cell* **57**, 273–289 (2015).
27. Lee, D. H. et al. A PP4 phosphatase complex dephosphorylates RPA2 to facilitate DNA repair via homologous recombination. *Nat. Struct. Mol. Biol.* **17**, 365–372 (2010).
28. Wang, S. et al. The PROTEIN PHOSPHATASE4 complex promotes transcription and processing of primary microRNAs in *Arabidopsis*. *Plant Cell* **31**, 486–501 (2019).
29. Wu, G., Rossidivito, G., Hu, T., Berlyand, Y. & Poethig, R. S. Traffic lines: new tools for genetic analysis in *Arabidopsis thaliana*. *Genetics* 200, 35–45 (2015).
30. Melamed-Bessudo, C., Yehuda, E., Stuitje, A. R. & Levy, A. A. A new seed-based assay for meiotic recombination in *Arabidopsis thaliana*. *Plant J.* **43**, 458–466 (2005).
31. Berchowitz, L. E. & Copenhaver, G. P. Fluorescent *Arabidopsis* tetrads: a visual assay for quickly developing large crossover and crossover interference data sets. *Nat. Protoc.* **3**, 41–50 (2008).
32. Ziolkowski, P. A. et al. Juxtaposition of heterozygous and homozygous regions causes reciprocal crossover remodelling via interference during *Arabidopsis meiosis*. *eLife* **4**, e03708 (2015).
33. Yelina, N. E. et al. DNA methylation epigenetically silences crossover hot spots and controls chromosomal domains of meiotic recombination in *Arabidopsis*. *Genes Dev.* **29**, 2183–2202 (2015).
34. Lawrence, E. J. et al. Natural variation in TBP-ASSOCIATED factor 4b controls meiotic crossover and germline transcription in *Arabidopsis*. *Curr. Biol.* **29**, 2676–2686 (2019).
35. Choi, K. et al. *Arabidopsis* meiotic crossover hot spots overlap with H2A.Z nucleosomes at gene promoters. *Nat. Genet.* **45**, 1327–1336 (2013).
36. Ziolkowski, P. A. et al. Natural variation and dosage of the HEI10 meiotic E3 ligase control *Arabidopsis* crossover recombination. *Genes Dev.* **31**, 306–317 (2017).
37. Crismani, W. et al. FANCM limits meiotic crossovers. *Science* **336**, 1588–1590 (2012).
38. Allen, R., Nakasugi, K., Doran, R. L., Millar, A. A. & Waterhouse, P. M. Facile mutant identification via a single parental backcross method and application of whole genome sequencing based mapping pipelines. *Front. Plant Sci.* **4**, 362 (2013).
39. Shi, Y. Serine/threonine phosphatases: mechanism through structure. *Cell* **139**, 468–484 (2009).
40. Gingras, A. C. et al. A novel, evolutionarily conserved protein phosphatase complex involved in cisplatin sensitivity. *Mol. Cell. Proteom.* **4**, 1725–1740 (2005).
41. Ramos, F., Villoria, M. T., Alonso-Rodríguez, E. & Clemente-Blanco, A. Role of protein phosphatases PP1, PP2A, PP4 and Cdc14 in the DNA damage response. *Cell Stress* **3**, 70–85 (2019).
42. Nakada, S., Chen, G. I., Gingras, A. C. & Durocher, D. PP4 is a γH2AX phosphatase required for recovery from the DNA damage checkpoint. *EMBO Rep.* **9**, 1019–1026 (2008).
43. Chowdhury, D. et al. PP4–phosphatase complex dephosphorylates γ-H2AX generated during DNA replication. *Mol. Cell* **31**, 33–46 (2008).
44. Merigliano, C. et al. A role for the twins protein phosphatase (PP2A–B55) in the maintenance of *Drosophila* genome integrity. *Genetics* **205**, 1151–1167 (2017).
45. Keogh, M. C. et al. A phosphatase complex that dephosphorylates γH2AX regulates DNA damage checkpoint recovery. *Nature* **439**, 497–501 (2006).

46. O'Neill, B. M. et al. Pph3–Psy2 is a phosphatase complex required for Rad53 dephosphorylation and replication fork restart during recovery from DNA damage. *Proc. Natl Acad. Sci. USA* **104**, 9290–9295 (2007).
47. Liu, J. et al. Protein phosphatase PP4 is involved in NHEJ-mediated repair of DNA double-strand breaks. *Cell Cycle* **11**, 2643–2649 (2012).
48. Falk, J. E., Chan, A. C., Hoffmann, E. & Hochwagen, A. A Mec1- and PP4-dependent checkpoint couples centromere pairing to meiotic recombination. *Dev. Cell* **19**, 599–611 (2010).
49. Pérez-Callejón, E. et al. Identification and molecular cloning of two homologues of protein phosphatase X from *Arabidopsis thaliana*. *Plant Mol. Biol.* **23**, 1177–1185 (1993).
50. Moorhead, G. B. G., De Wever, V., Templeton, G. & Kerk, D. Evolution of protein phosphatases in plants and animals. *Biochem. J.* **417**, 401–409 (2009).
51. Su, C. et al. The protein phosphatase 4 and SMEK1 complex dephosphorylates HYL1 to promote miRNA biogenesis by antagonizing the MAPK cascade in Arabidopsis. *Dev. Cell* **41**, 527–539 (2017).
52. de Felippes, F. F., Wang, J. & Weigel, D. MIGS: miRNA-induced gene silencing. *Plant J.* **70**, 541–547 (2012).
53. Klimyuk, V. I. & Jones, J. D. AtDMC1, the *Arabidopsis* homologue of the yeast DMC1 gene: characterization, transposon-induced allelic variation and meiosis-associated expression. *Plant J.* **11**, 1–14 (1997).
54. Lim, E. C. et al. DeepTetrad: high-throughput image analysis of meiotic tetrads by deep learning in *Arabidopsis thaliana*. *Plant J.* **101**, 473–483 (2020).
55. Rowan, B. A., Patel, V., Weigel, D. & Schneeberger, K. Rapid and inexpensive whole-genome genotyping-by-sequencing for crossover localization and fine-scale genetic mapping. *G3 (Bethesda)* **5**, 385–398 (2015).
56. Choi, K. et al. Recombination rate heterogeneity within *Arabidopsis* disease resistance genes. *PLoS Genet.* **12**, e1006179 (2016).
57. Choi, K. et al. Nucleosomes and DNA methylation shape meiotic DSB frequency in *Arabidopsis thaliana* transposons and gene regulatory regions. *Genome Res.* **28**, 532–546 (2018).
58. Zhang, J. et al. A multiprotein complex regulates interference-sensitive crossover formation in rice. *Plant Physiol.* **181**, 221–235 (2019).
59. Macaisne, N., Vignard, J. & Mercier, R. SHOC1 and PTD form an XPF–ERCC1-like complex that is required for formation of class I crossovers. *J. Cell Sci.* **124**, 2687–2691 (2011).
60. Ueki, Y. et al. A consensus binding motif for the PP4 protein phosphatase. *Mol. Cell* **76**, 953–964 (2019).
61. Fernandes, J. B., Seguela-Arnaud, M., Larcheveque, C., Lloyd, A. H. & Mercier, R. Unleashing meiotic crossovers in hybrid plants. *Proc. Natl Acad. Sci. USA* **115**, 2431–2436 (2017).
62. Wijnker, E. et al. The Cdk1/Cdk2 homolog CDKA;1 controls the recombination landscape in Arabidopsis. *Proc. Natl Acad. Sci. USA* **116**, 12534–12539 (2019).
63. He, Y. et al. Genomic features shaping the landscape of meiotic double-strand-break hotspots in maize. *Proc. Natl Acad. Sci. USA* **114**, 12231–12236 (2017).
64. Liu, S. et al. Mu transposon insertion sites and meiotic recombination events co-localize with epigenetic marks for open chromatin across the maize genome. *PLoS Genet.* **5**, e1000733 (2009).
65. Underwood, C. J. et al. Epigenetic activation of meiotic recombination near *Arabidopsis thaliana* centromeres via loss of H3K9me2 and non-CG DNA methylation. *Genome Res.* **28**, 519–531 (2018).
66. Chelysheva, L. et al. The *Arabidopsis* HEI10 is a new ZMM protein related to Zip3. *PLoS Genet.* **8**, e1002799 (2012).
67. Wang, K. et al. The role of rice HEI10 in the formation of meiotic crossovers. *PLoS Genet.* **8**, e1002809 (2012).
68. Reynolds, A. et al. RNF212 is a dosage-sensitive regulator of crossing-over during mammalian meiosis. *Nat. Genet.* **45**, 269–278 (2013).
69. Qiao, H. et al. Antagonistic roles of ubiquitin ligase HEI10 and SUMO ligase RNF212 regulate meiotic recombination. *Nat. Genet.* **46**, 194–199 (2014).
70. Woglar, A. & Villeneuve, A. M. Dynamic architecture of DNA repair complexes and the synaptonemal complex at sites of meiotic recombination. *Cell* **173**, 1678–1691 (2018).
71. Snowden, T., Acharya, S., Butz, C., Berardini, M. & Fishel, R. hMSH4–hMSH5 recognizes Holliday junctions and forms a meiosis-specific sliding clamp that embraces homologous chromosomes. *Mol. Cell* **15**, 437–451 (2004).
72. Jessop, L., Rockmill, B., Roeder, G. S. & Lichten, M. Meiotic chromosome synapsis-promoting proteins antagonize the anti-crossover activity of sgs1. *PLoS Genet.* **2**, e155 (2006).
73. Oh, S. D., Lao, J. P., Taylor, A. F., Smith, G. R. & Hunter, N. RecQ helicase, Sgs1, and XPF family endonuclease, Mus81–Mms4, resolve aberrant joint molecules during meiotic recombination. *Mol. Cell* **31**, 324–336 (2008).
74. Manhart, C. M. et al. The mismatch repair and meiotic recombination endonuclease Mlh1–Mlh3 is activated by polymer formation and can cleave DNA substrates in *trans*. *PLoS Biol.* **15**, e2001164 (2017).
75. Zakharyevich, K., Tang, S., Ma, Y. & Hunter, N. Delineation of joint molecule resolution pathways in meiosis identifies a crossover-specific resolvase. *Cell* **149**, 334–347 (2012).
76. Ranjha, L., Anand, R. & Cejka, P. The Saccharomyces cerevisiae Mlh1–Mlh3 heterodimer is an endonuclease that preferentially binds to Holliday junctions. *J. Biol. Chem.* **289**, 5674–5686 (2014).
77. Wijeratne, A. J., Chen, C., Zhang, W., Timofejeva, L. & Ma, H. The *Arabidopsis thaliana* parting dancers gene encoding a novel protein is required for normal meiotic homologous recombination. *Mol. Biol. Cell* **17**, 1331–1343 (2006).
78. Lu, P., Wijeratne, A. J., Wang, Z., Copenhaver, G. P. & Ma, H. *Arabidopsis* PTD is required for type I crossover formation and affects recombination frequency in two different chromosomal regions. *J. Genet. Genomics* **41**, 165–175 (2014).
79. De Muyt, A. et al. A meiotic XPF–ERCC1-like complex recognizes joint molecule recombination intermediates to promote crossover formation. *Genes Dev.* **32**, 283–296 (2018).
80. Arora, K. & Corbett, K. D. The conserved XPF:ERCC1-like Zip2:Spo16 complex controls meiotic crossover formation through structure-specific DNA binding. *Nucleic Acids Res.* **47**, 2365–2376 (2019).
81. Sato-Carlton, A. et al. Protein phosphatase 4 promotes chromosome pairing and synapsis, and contributes to maintaining crossover competence with increasing age. *PLoS Genet.* **10**, e1004638 (2014).
82. Henderson, K. A., Kee, K., Maleki, S., Santini, P. A. & Keeney, S. Cyclin-dependent kinase directly regulates initiation of meiotic recombination. *Cell* **125**, 1321–1332 (2006).
83. Lam, I. & Keeney, S. Mechanism and regulation of meiotic recombination initiation. *Cold Spring Harb. Perspect. Biol.* **7**, a016634 (2014).
84. Valentin, G., Schwob, E. & Della Seta, F. Dual role of the Cdc7-regulatory protein Dbf4 during yeast meiosis. *J. Biol. Chem.* **281**, 2828–2834 (2006).
85. Sasanuma, H. et al. Cdc7-dependent phosphorylation of Mer2 facilitates initiation of yeast meiotic recombination. *Genes Dev.* **22**, 398–410 (2008).
86. Wan, L. et al. Cdc28–Clb5 (CDK-S) and Cdc7–Dbf4 (DDK) collaborate to initiate meiotic recombination in yeast. *Genes Dev.* **22**, 386–397 (2008).
87. Matos, J. et al. Dbf4-Dependent Cdc7 kinase links DNA replication to the segregation of homologous chromosomes in meiosis I. *Cell* **135**, 662–678 (2008).
88. Chen, X. et al. Phosphorylation of the synaptonemal complex protein Zip1 regulates the crossover/noncrossover decision during yeast meiosis. *PLoS Biol.* **13**, e1002329 (2015).
89. Keeney, S., Lange, J. & Mohibullah, N. Self-organization of meiotic recombination initiation: general principles and molecular pathways. *Annu. Rev. Genet.* **48**, 187–214 (2014).
90. Nowack, M. K. et al. Genetic framework of cyclin-dependent kinase function in *Arabidopsis*. *Dev. Cell* **22**, 1030–1040 (2012).
91. Culligan, K. M. & Britt, A. B. Both ATM and ATR promote the efficient and accurate processing of programmed meiotic double-strand breaks. *Plant J.* **55**, 629–638 (2008).
92. Garcia, V. et al. AtATM is essential for meiosis and the somatic response to DNA damage in plants. *Plant Cell* **15**, 119–132 (2003).
93. Yao, Y. et al. ATM promotes RAD51-mediated meiotic DSB repair by inter-sister-chromatid recombination in *Arabidopsis*. *Front. Plant Sci.* **11**, 839 (2020).
94. Villoria, M. T. et al. PP4 phosphatase cooperates in recombinational DNA repair by enhancing double-strand break end resection. *Nucleic Acids Res.* **47**, 10706–10727 (2019).
95. Chelysheva, L. et al. Zip4/Spo22 is required for class I CO formation but not for synapsis completion in *Arabidopsis thaliana*. *PLoS Genet.* **3**, e83 (2007).
96. van Tol, N., Rolloos, M., van Loon, P. & van der Zaal, B. J. MeioSeed: a CellProfiler-based program to count fluorescent seeds for crossover frequency analysis in *Arabidopsis thaliana*. *Plant Methods* **14**, 32 (2018).
97. Carpenter, A. E. et al. CellProfiler: image analysis software for identifying and quantifying cell phenotypes. *Genome Biol.* **7**, R100 (2006).
98. Zhang, X., Henriques, R., Lin, S. S., Niu, Q. W. & Chua, N. H. *Agrobacterium*-mediated transformation of *Arabidopsis thaliana* using the floral dip method. *Nat. Protoc.* **1**, 641–646 (2006).
99. Chelysheva, L. et al. An easy protocol for studying chromatin and recombination protein dynamics during *Arabidopsis thaliana* meiosis: immunodetection of cohesins, histones and MLH1. *Cytogenet. Genome Res.* **129**, 143–153 (2010).
100. Lambing, C., Kuo, P. C., Tock, A. J., Topp, S. D. & Henderson, I. R. ASY1 acts as a dosage-dependent antagonist of telomere-led recombination and mediates crossover interference in *Arabidopsis*. *Proc. Natl Acad. Sci. USA* **24**, 13647–13658 (2020).

101. Sanchez-Moran, E., Santos, J.-L., Jones, G. H. & Franklin, F. C. H. ASY1 mediates AtDMC1-dependent interhomolog recombination during meiosis in *Arabidopsis*. *Genes Dev.* **21**, 2220–2233 (2007).
102. Higgins, J. D., Sanchez-Moran, E., Armstrong, S. J., Jones, G. H. & Franklin, F. C. H. The *Arabidopsis* synaptonemal complex protein ZYP1 is required for chromosome synapsis and normal fidelity of crossing over. *Genes Dev.* **19**, 2488–2500 (2005).
103. Hwang, I. & Sheen, J. Two-component circuitry in *Arabidopsis* cytokinin signal transduction. *Nature* **413**, 383–389 (2001).
104. Xue, Y. et al. GPS 2.1: Enhanced prediction of kinase-specific phosphorylation sites with an algorithm of motif length selection. *Protein Eng. Des. Sel.* **24**, 255–260 (2011).

Acknowledgements

We thank G. Copenhaver, A. Levy and S. Poethig for FTLs/CTLs, R. Mercier for *fancm-1*, L. Ziolkowska and C. Underwood for helping grow the EMS population, M. Grelon for MLH1 antibodies, C. Franklin for ASY1, ZYP1 and RAD51 antibodies and the Gurdon Institute for access to microscopes. This work was funded by the Suh Kyungbae Foundation (Jaeil Kim, Juhyun Kim, J.P., E.-J.K., H.K., D.B., Y.M.P. and K.C.), Next-Generation BioGreen 21 Program PJ01337001 (Jaeil Kim, Juhyun Kim, J.P., E.-J.K., H.K., D.B., Y.M.P. and K.C.) and PJ01342301 (H.S.C., S.L. and I.H.), Rural Development Administration, Basic Science Research Program through the National Research Foundation of Korea (NRF) funded by the Ministry of Education NRF-2020R1A2C2007763 (H.K., D.B. and K.C.), Marie Curie International Training Network 'COMREC' (DN), Biotechnology and Biological Sciences Research Council grant EpiSpiX BB/N007557/1 (X.Z. and I.H.), Biotechnology and Biological Sciences Research Council ERA-CAPs grant BB/M004937/1 (C.L. and I.H.) and European Research Council Consolidator Award ERC-2015-CoG-681987 'SynthHotSpot' (C.L., A.J.T. and I.H.).

Author contributions

Design and conception of experiments: D.C.N., Jaeil Kim, C.L., Juhyun Kim, J.P., E.-J.K., P.K., K.C. and I.H. Acquisition and analysis of data: D.C.N., Jaeil Kim, C.L., Juhyun Kim, J.P., H.S.C., H.K., D.B., Y.M.P., P.K., S.L., A.J.T., X.Z., I.H. and K.C. Writing of the manuscript: D.C.N., Jaeil Kim, C.L., Juhyun Kim, K.C. and I.H.

Competing interests

The authors declare no competing interests.

Additional information

Extended data is available for this paper at https://doi.org/10.1038/s41477-021-00889-y.

Supplementary information The online version contains supplementary material available at https://doi.org/10.1038/s41477-021-00889-y.

Correspondence and requests for materials should be addressed to K.C. or I.R.H.

Peer review information *Nature Plants* thanks the anonymous reviewers for their contribution to the peer review of this work.

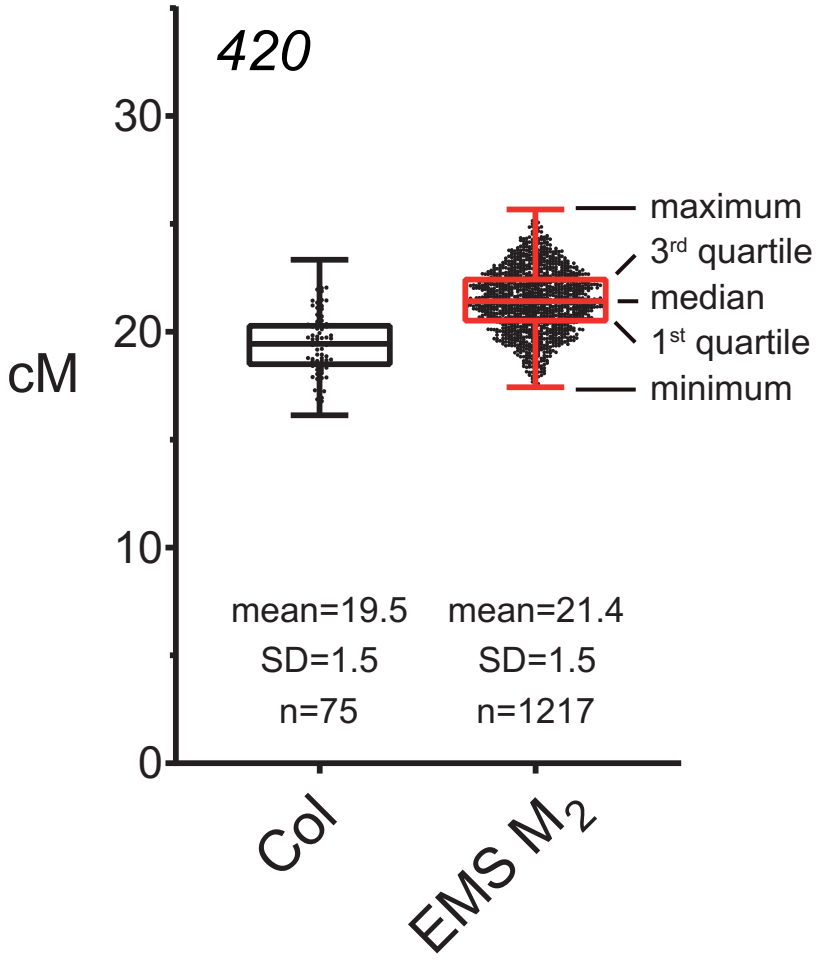

Extended Data Fig. 1 | *420* crossover frequency in wild type and M_2 plants derived from the EMS population. Box and whisker plot showing *420* crossover frequency (cM) for wild type (Col/Col) *420/++* plants (n=75) and EMS-treated M_2 *420/++* plants (n=1,217). Black dots indicate *420* crossover frequency in individual plants. Horizontal lines of black (wild type, Col) and red (EMS M_2) box plots represent maximum, 3rd quartile, median, 1st quartile and minimum in *420* cM, respectively. In this study, wild type plants show a mean value of 19.5 cM (standard deviation=1.5) within *420*, and the majority (81.4%, 991/1,217) of M_2 plants display *420* crossover frequency within the range of 18-22 cM (Mean=21.4 cM, SD=1.5). *420* crossover frequency in M_2 plants was significantly increased compared to wild type (one-sided Welch's t-test $P=2.2\times10^{-16}$), which may have been caused by heterozygous EMS polymorphisms.

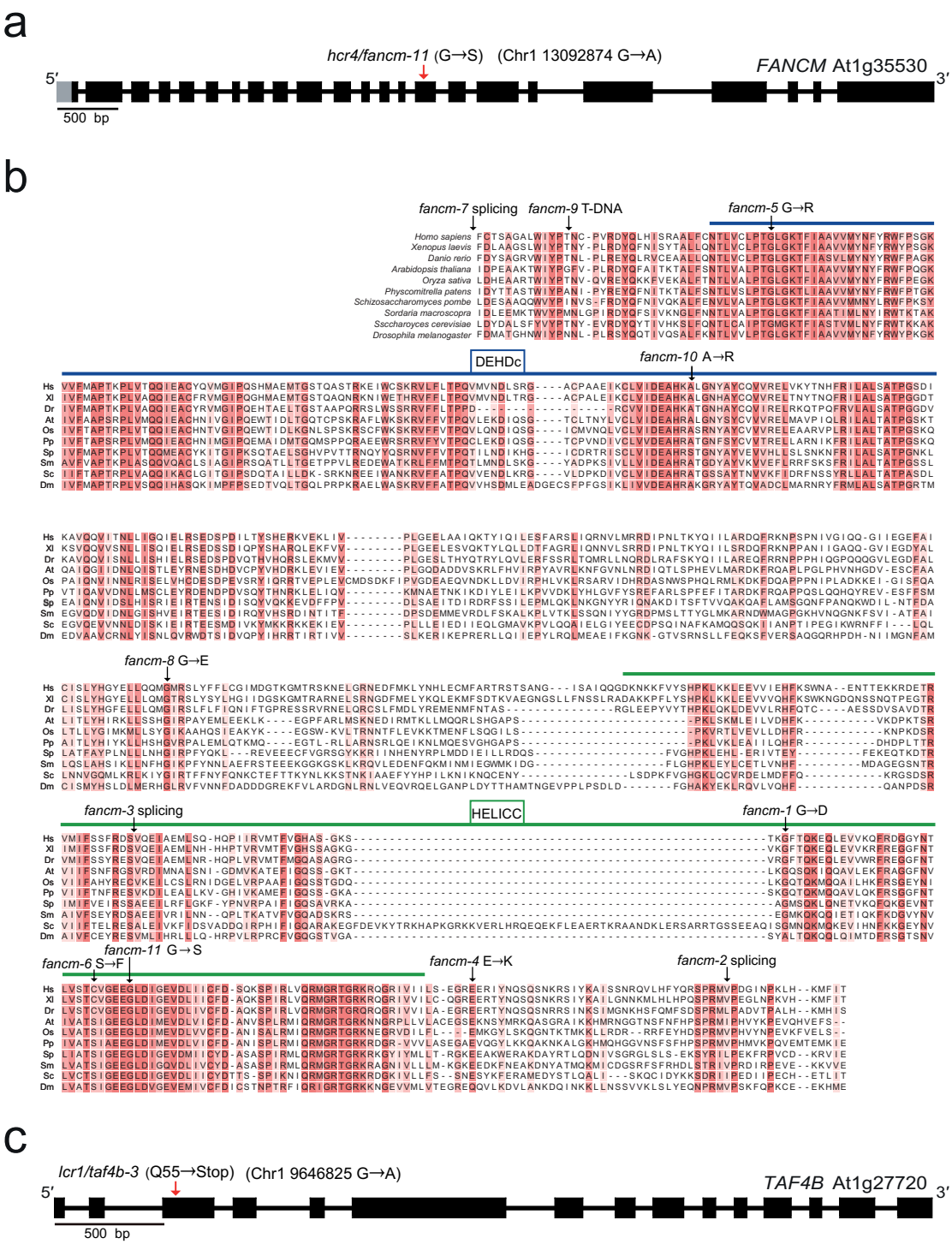

Extended Data Fig. 2 | EMS mutations identified in *FANCM* (*hcr4*) and *TAF4b* (*lcr1*). a, *FANCM* gene structure is shown, including the EMS mutation site in *hcr4/fancm-11*. The red arrow indicates the G to A substitution within exon 15, which causes a G to S amino acid substitution. Exons are shown as boxes (black=CDS, grey=UTR). Scale bar=0.5 kb. **b**, Multiple sequence alignment of the DEHDc (blue line) and HELICC (green line) domains of FANCM in different species. The mutation positions of the *fancm-1* to *fancm-10* alleles that were previously identified, and *fancm-11* (*hcr4*), are shown. The *fancm-11* mutation is located in a conserved motif within the SF2 helicase domain (bold arrow). **c**, Gene structure of *TAF4b* is shown with the location of the *lcr1* (*taf4b-3*) mutation indicated in exon 3 (red arrow), which causes a premature stop codon.

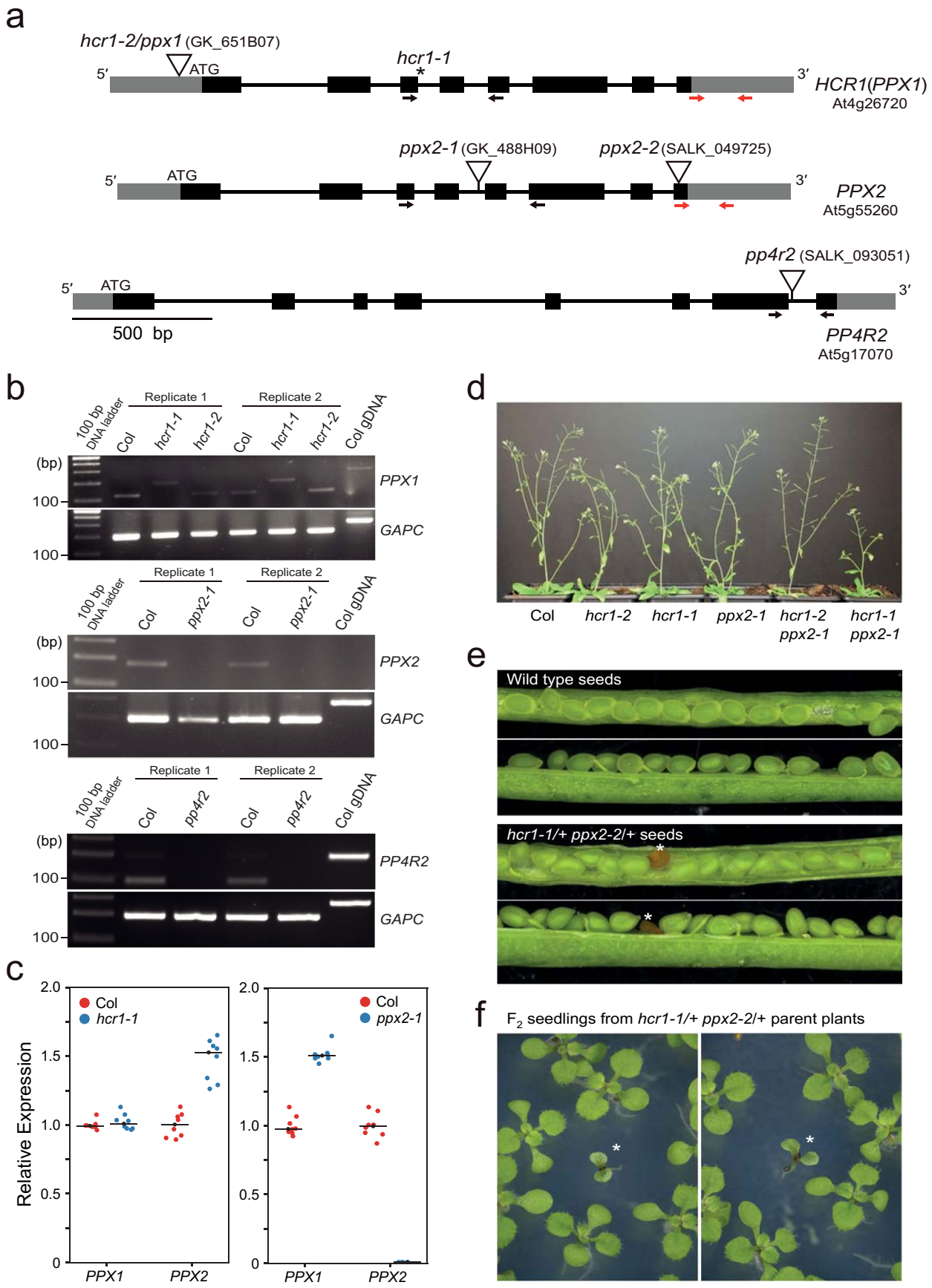

Extended Data Fig. 3 | See next page for caption.

Extended Data Fig. 3 | T-DNA insertions in Arabidopsis *PP4/PPX* complex genes. a, The gene structures of *PPX1* (At4g26720), *PPX2* (At5g55260) and *PP4R2* (At5g17070) are shown. Exons are shown as boxes (black=CDS, grey=UTR). Scale bar=0.5 kb. The EMS induced *hcr1-1* mutation is located at the splice donor site of the 3rd intron, shown by the asterisk. The red arrows indicate the location of primers for RT-qPCR in *PPX1* and *PPX2*. The *hcr1-2* T-DNA (GK_651B07) insertion position in the 5´-UTR is indicated. The position of the *ppx2-1* (GK_488H09), *ppx2-2* (SALK_049725), and *pp4r2* (SALK_093051) T-DNA insertions are shown, which are located in the 4th intron, 8th exon and 7th intron, respectively. The arrows spanning the *ppx2* and *pp4r2* T-DNA insertions indicate primer positions used for RT-PCR. **b**, RT-PCR amplification and quantification for *PPX1, PPX2* and *PP4R2* mRNA expression in wild type Col, *hcr1-1*, *ppx1-2*, *ppx2-1* and *pp4r2*. Floral cDNA from two biological replicates were evaluated by RT-PCR amplification for *PPX1*, *PPX2*, *PP4R2* (shown in a) and *GAPC* expression. RT-PCR amplicon sizes for wild type, *hcr1-1*, *ppx1-2*, *ppx2-1*, *pp4r2* cDNAs and wild type genomic DNA (positive/negative control) are shown. **c**, Plot showing RT-qPCR enrichment of *PPX1* and *PPX2* in *hcr1-1* and *ppx2-1*. Relative transcript levels of *PPX1* and *PPX2* were measured in wild type, *hcr1-1*, and *ppx2-1* using qRT-PCR. *TUB2* was used for normalization. The y axis indicates fold-enrichment of *PPX1* and *PPX2* transcript levels, compared to *PPX1* and *PPX2* in wild type. RT-qPCR reactions of two technical replicates for each of four biological samples were shown as dots. Mean values are indicated by horizontal lines. Significance between wild type and mutants was assessed by one-sided Welch's t-tests. The *P* values between Col and *hcr1-1* for *PPX1* was 0.186, for *PPX2* was 3.49×10^{-5}; between Col and *ppx2-1* for *PPX1* was 1.77×10^{-10} and for *PPX2* was 3.64×10^{-9}. Asterisks indicate $P<0.001$. **d**, Photograph showing developmental phenotypes of wild type, *hcr1-2*, *hcr1-1*, *ppx2-1*, *hcr1-2 ppx2-1* and *hcr1-1 ppx2-1* grown alongside one another. **e**, Photograph showing seeds of wild type and *hcr1-1/+ ppx2-2/+* plants. Asterisks indicate defective seeds. **f**, Photograph showing F_2 seedlings grown from self-fertilization of F_1 *hcr1-1/+ ppx2-2/+* plants, with asterisks indicating developmentally delayed seedlings.

a

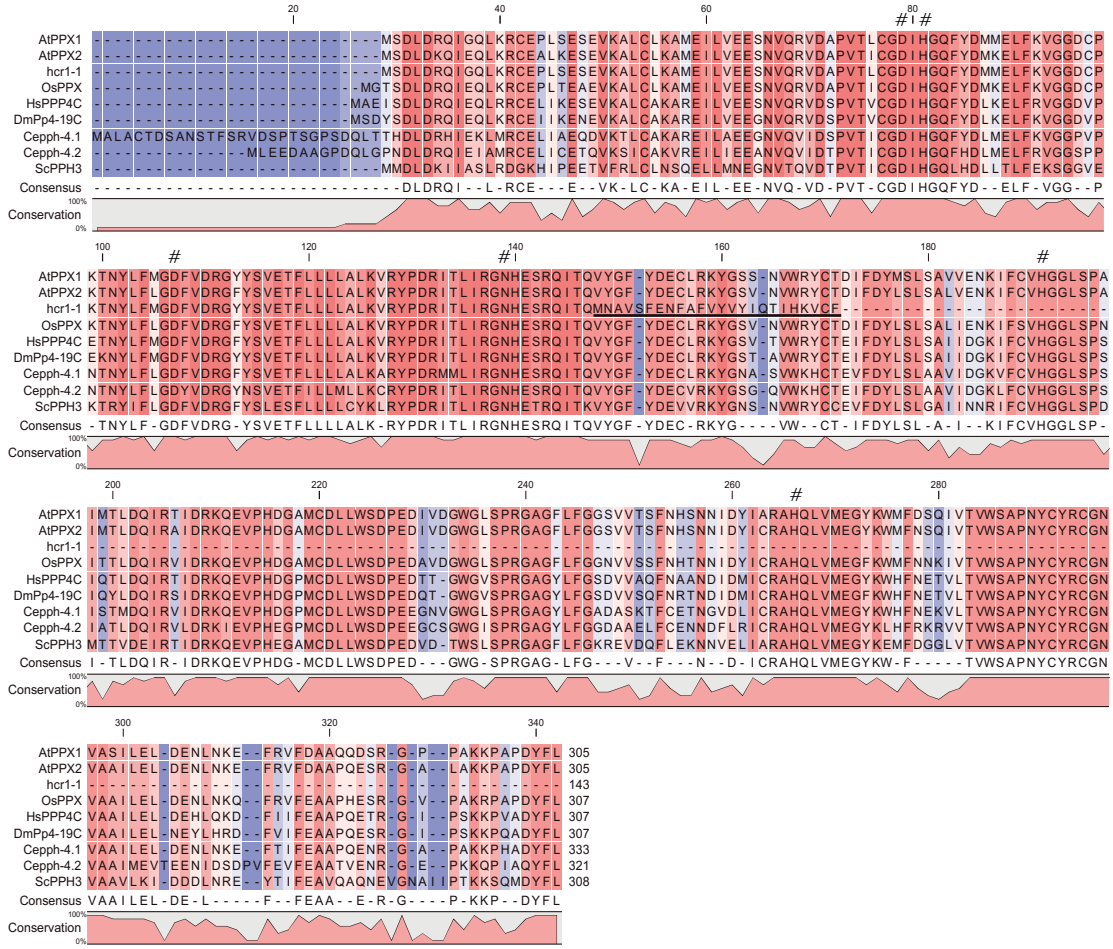

b

	AtPPX1	AtPPX2	OsPPX	HsPPP4C	DmPp4-19C	Cepph-4.1	Cepph-4.2	ScPPH3
AtPPX1		93.77	88.93	79.55	78.25	67.57	64.49	64.08
AtPPX2	93.77		92.18	81.82	79.87	69.67	65.11	64.08
OsPPX	88.93	92.18		81.17	80.84	70.27	65.84	63.34
HsPPP4C	79.55	81.82	81.17		91.53	74.47	69.88	62.18
DmPp4-19C	78.25	79.87	80.84	91.53		72.97	68.63	60.90
Cepph-4.1	67.57	69.67	70.27	74.47	72.97		70.83	57.57
Cepph-4.2	64.49	65.11	65.84	69.88	68.63	70.83		54.15
ScPPH3	64.08	64.08	63.34	62.18	60.90	57.57	54.15	

Extended Data Fig. 4 | Alignment of PP4 homolog protein sequences from diverse eukaryotes. a, Amino acid sequence alignment of AtPPX1, the predicted *hcr1-1* truncated protein, AtPPX2 and PP4 homologs from different eukaryotic species. The predicted *hcr1-1* truncated protein consisting of 143 residues is shown. The underlined region indicates amino acids generated due to the retention of the 3rd intron. Hash symbols indicate the locations of conserved PP4 catalytic motifs (GDXHG, GDXVDRG and GNHE) and the histidine (H) residues required for metal binding in C-terminal region. **b**, As for a, but showing percent identity of amino acid sequence between PP4 homologs.

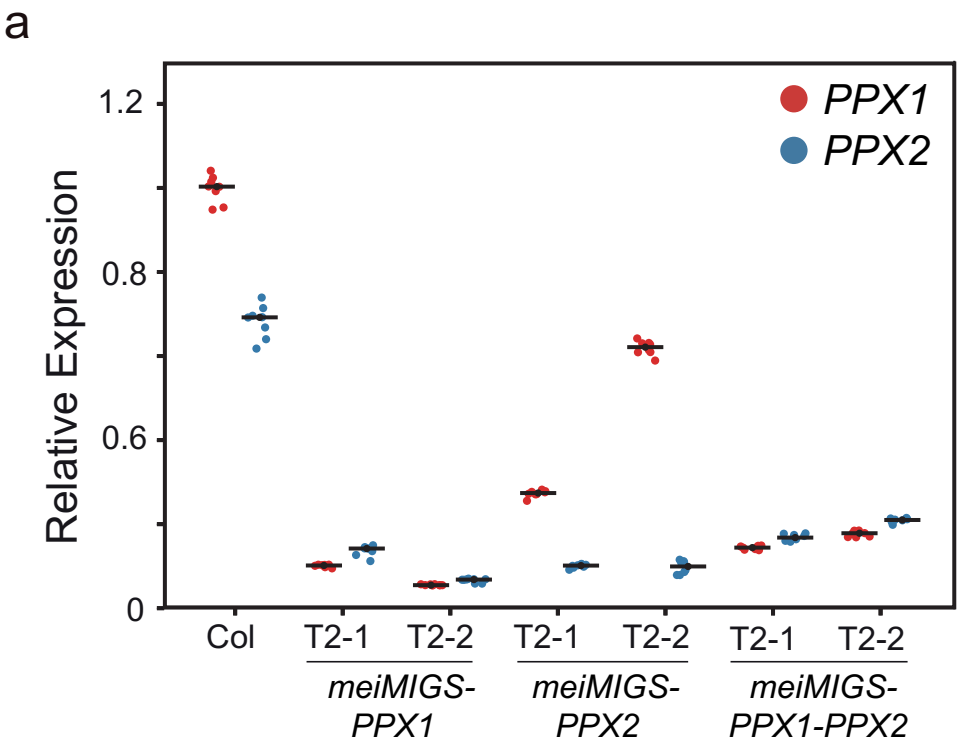

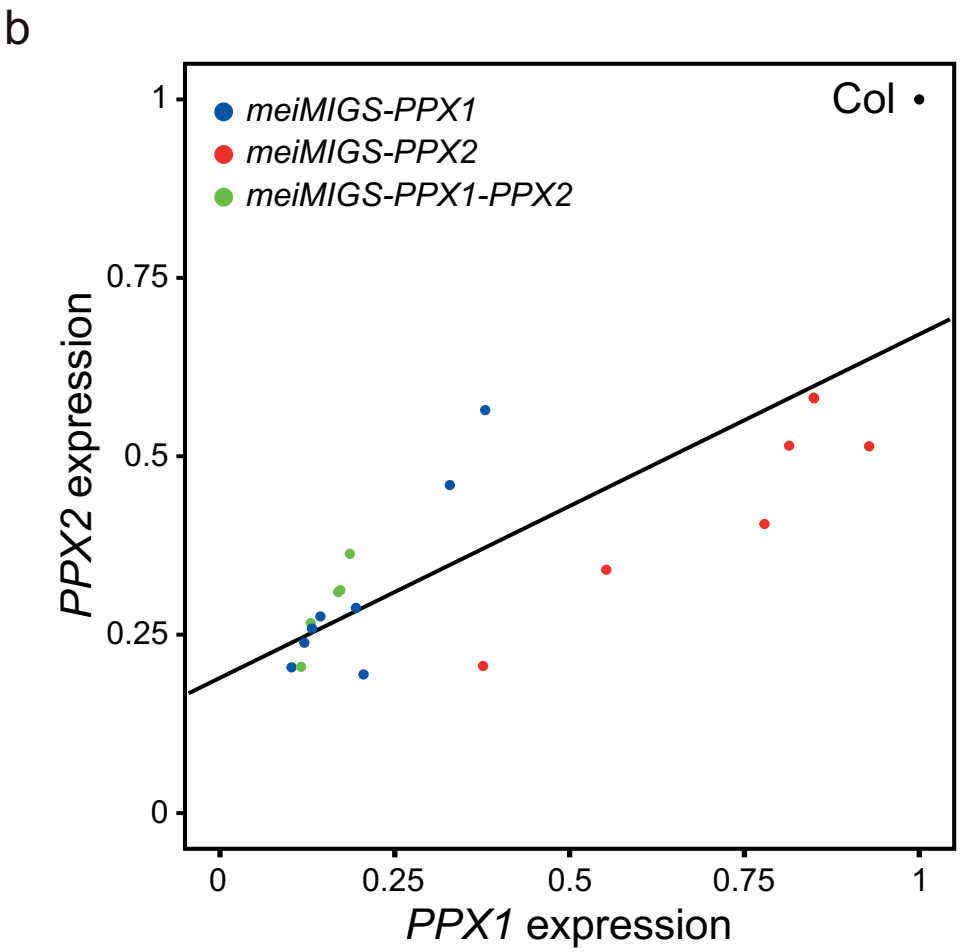

Extended Data Fig. 5 | See next page for caption.

Extended Data Fig. 5 | Meiosis-specific knockdown of *PPX1* and *PPX2* in *meiMIGS* transgenic plants. a, qRT-PCR analysis of *PPX1/HCR1* and *PPX2* transcripts in floral buds of wild type and *meiMIGS-PPX1*, *meiMIGS-PPX2* and *meiMIGS-PPX1-PPX2* T_2 transgenic lines. The y axis indicates fold-enrichment of *PPX1* and *PPX2* transcripts, compared to *PPX1* in wild type. *DMC1* was used as a meiotic gene for normalization. Replicate measurements are shown as dots and mean values shown by horizontal lines. **b**, Correlation between *PPX1* and *PPX2* transcript levels in wild type, *meiMIGS-PPX1*, *meiMIGS-PPX2*, and *meiMIGS-PPX1-PPX2* lines. The x and y axis indicate relative *PPX1* and *PPX2* transcript levels in *meiMIGS-PPX1* (blue), *meiMIGS-PPX2* (red), and *meiMIGS-PPX1-PPX2* (green) lines respectively, compared to *PPX1* and *PPX2* expressions in wild type Col plant. The correlation coefficient between *PPX1* and *PPX2* expression values across these samples was r=0.80, which was significantly different than expected if there were no relationship (P value=1.21×10^{-5}).

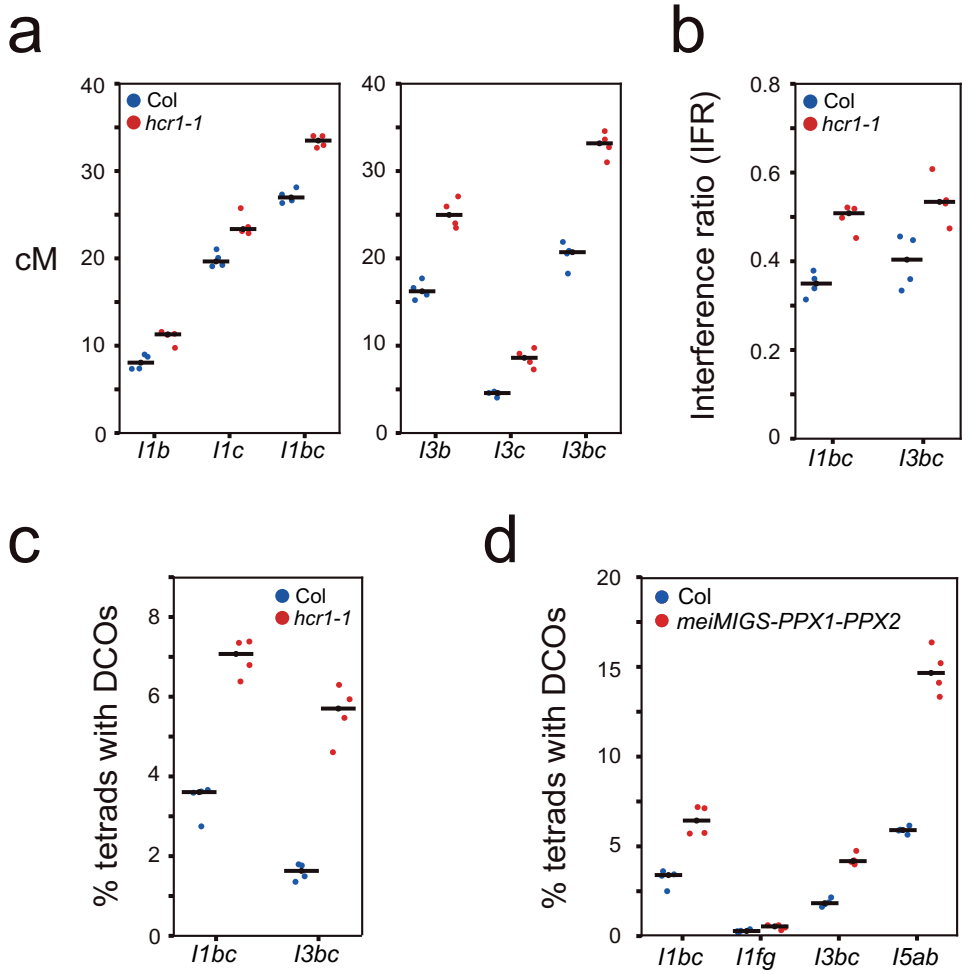

Extended Data Fig. 6 | Crossover frequency and interference measured in wild type and *hcr1-1* using fluorescent pollen. a, Crossover frequency measured using the pollen FTLs *I1bc* and *I3bc* from wild type and *hcr1-1*. Crossover frequency in each interval of the three-color FTLs was measured using the DeepTetrad pipeline[3] (Supplementary Table 20). **b**, Crossover interference ratio measured using FTL pollen tetrads in wild type and *hcr1-1*. Crossover interference ratio (IFR) were calculated using the DeepTetrad pipeline. **c**, Plots showing the % of tetrads containing double crossovers, using data from the three-color FTL intervals in wild type and *hcr1-1*. **d**, As for c, but showing FTL data from the *I1bc, I1fg, I3bc* and *I5ab* intervals in wild type and *meiMIGS-PPX1-PPX2*. Tetrads were classified into 12 fluorescence classes (A-L) by DeepTetrad. Mean values are indicated by horizontal lines.

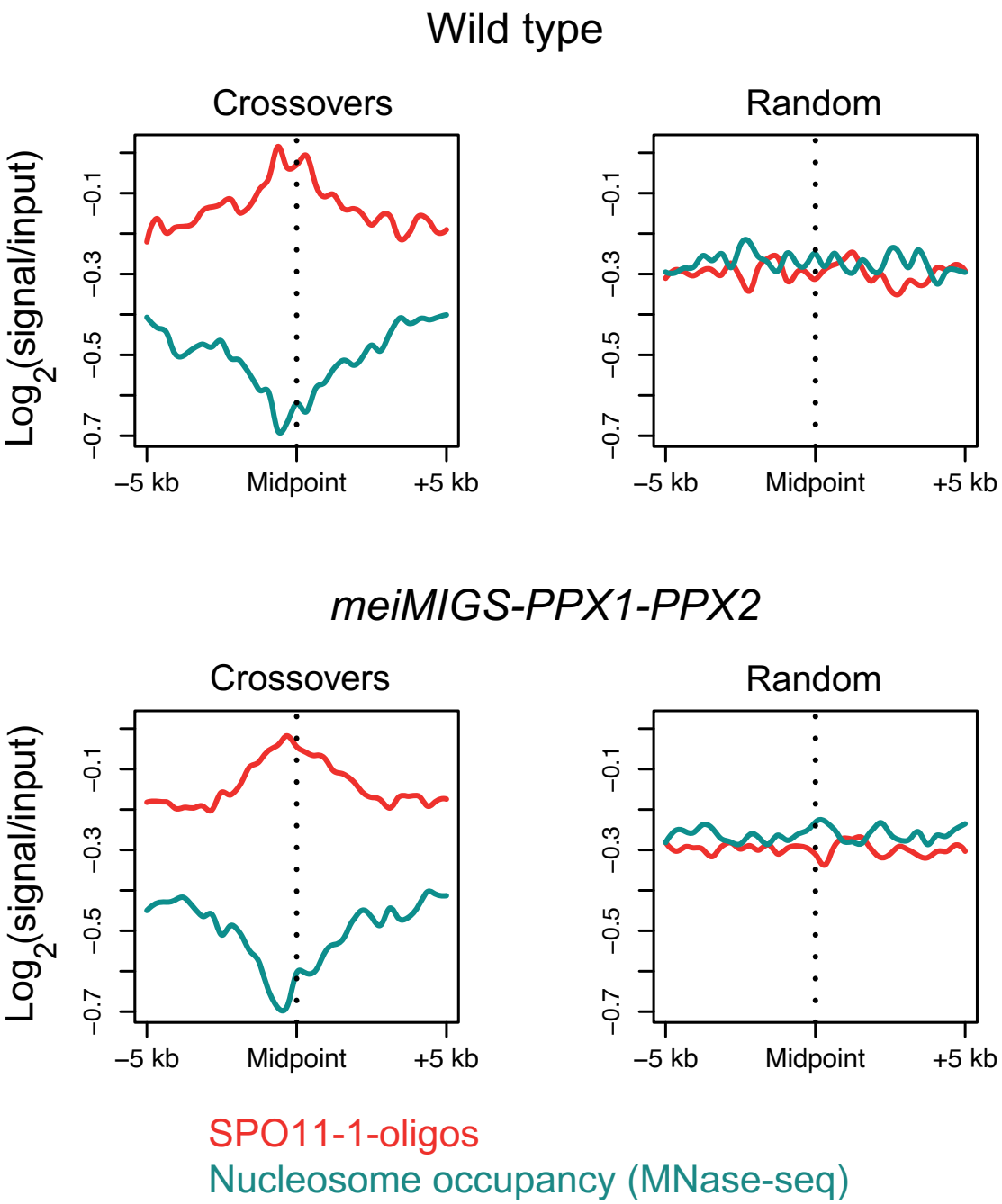

Extended Data Fig. 7 | SPO11-1-oligonucleotides and nucleosome occupancy around wild type and *meiMIGS-PPX1-PPX2* crossovers. 10 kb windows surrounding crossover midpoints identified from wild type or *meiMIGS-PPX1-PPX2* plants, or the same number of randomly selected positions, were analysed for SPO11-1-oligos (log_2(SPO11-1-oligos/gDNA), red) or nucleosome occupancy (log_2(MNase-seq/gDNA), blue).

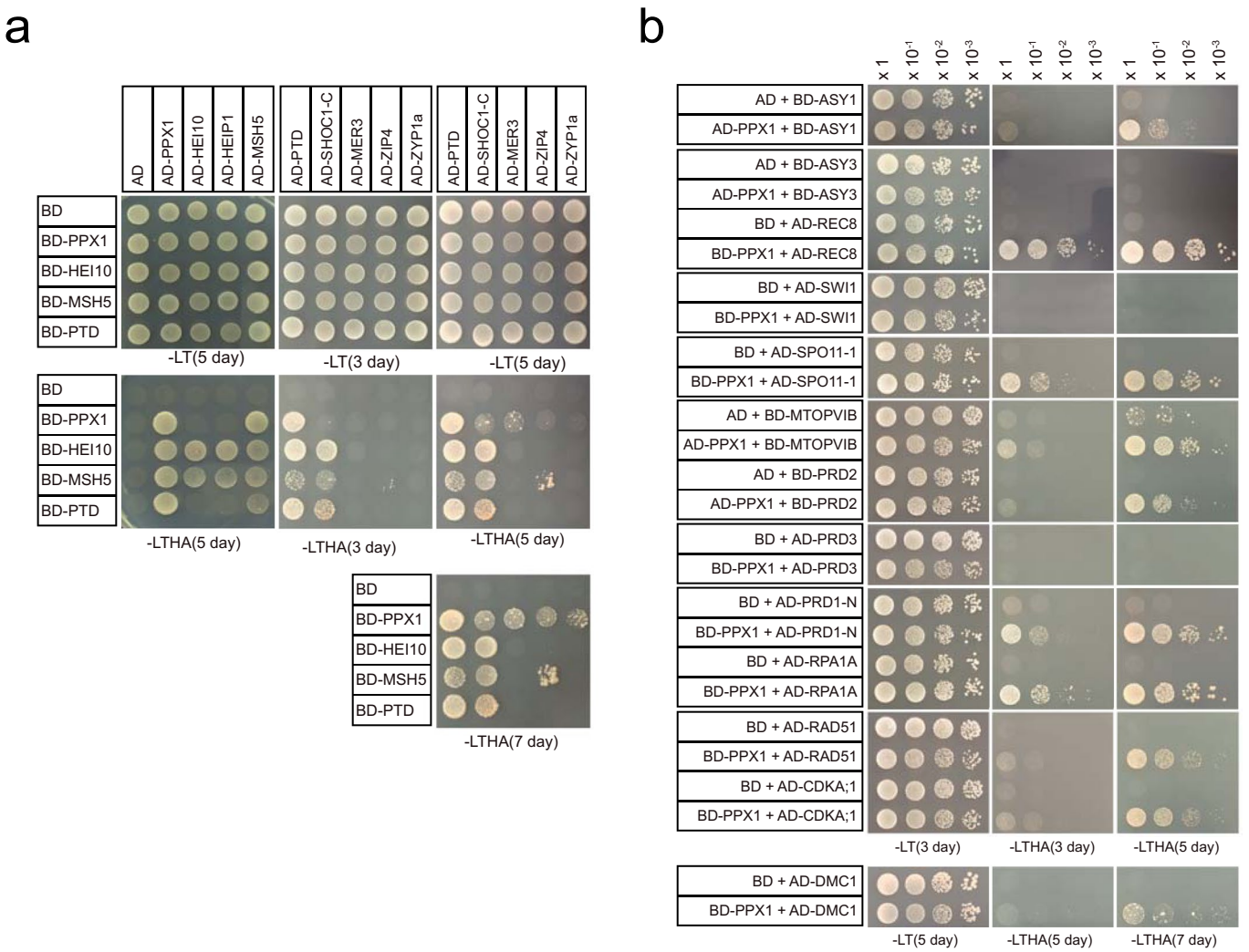

Extended Data Fig. 8 | Yeast two hybrid assays showing interactions of HCR1/PPX1 with meiotic proteins. a, Yeast two hybrid assays testing interaction between HCR1/PPX1 and Class I (ZMM) proteins. The yeast co-transformants were grown until $OD_{600} = 1$ and spotted on synthetic dropout media (SD) lacking leucine/tryptophan (-LT) and leucine/trptophan/histidine/adenine (-LTHA) for 3, 5 or 7 days. **b**, Yeast two hybrid assays of HCR1/PPX1 and meiotic proteins involved in axis formation, DSB formation and DNA repair. The yeast transformants were grown until $OD_{600} = 1$, then diluted 10-, 100- and 1,000-fold in water, and spotted on SD (-LT) and SD (-LTHA) plates to examine growth in 3, 5, or 7 days (Supplementary Table 23).

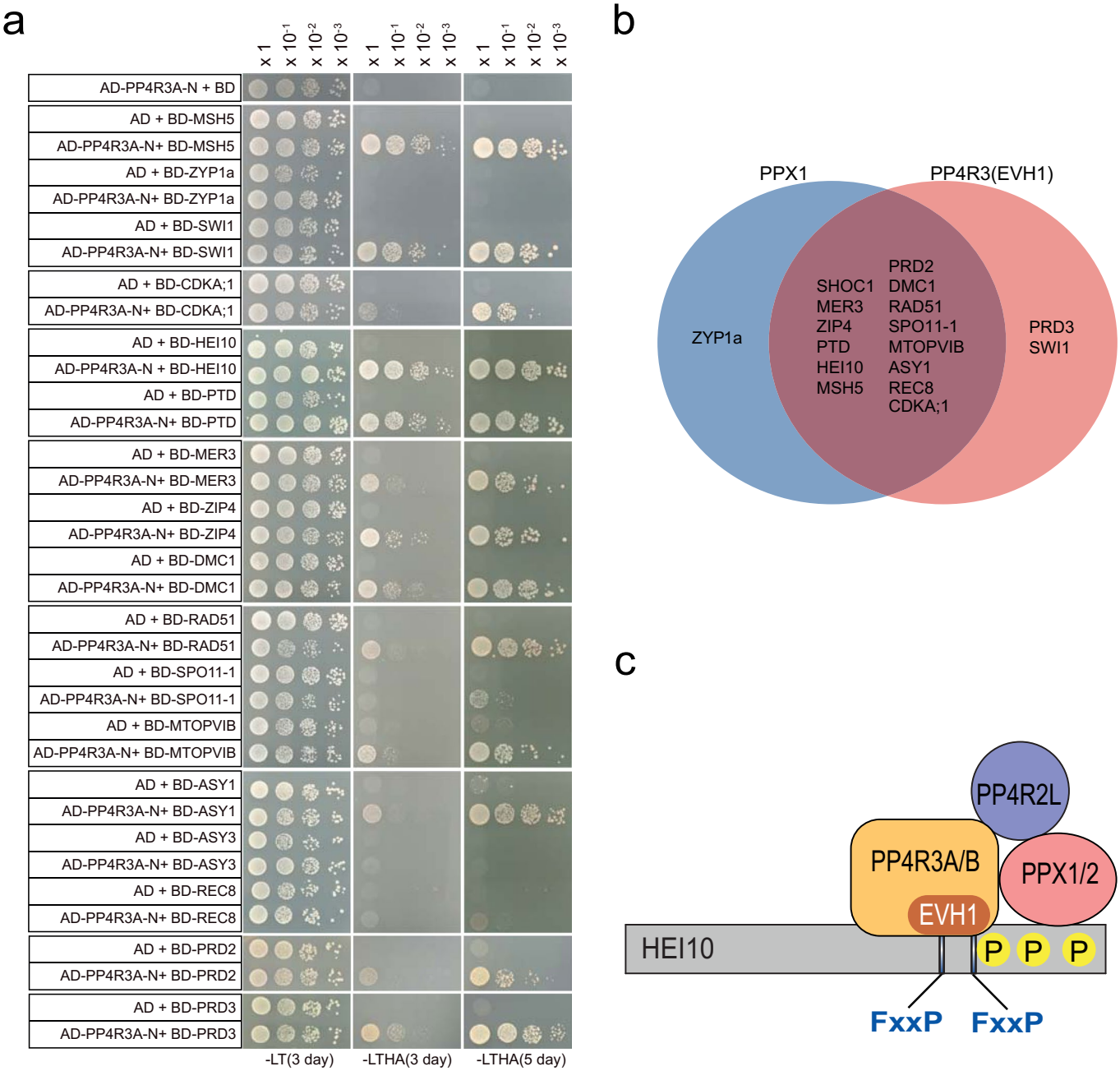

Extended Data Fig. 9 | The EVH1 domain of Arabidopsis PP4R3A interacts with meiotic proteins. a, Yeast two-hybrid assays testing interaction between the PP4R3A EVH1 domain and meiotic proteins. PP4R3A-N indicates the PP4R3A N-terminal region (1-166 aa) containing the EVH1 domain. The yeast co-transformants were grown until $OD_{600} = 1$ and spotted on synthetic dropout media (SD) lacking leucine/tryptophan (-LT) and leucine/trptophan/histidine/adenine (-LTHA) for 3 and 5 days. The yeast transformants were grown until $OD_{600} = 1$, then diluted 10-, 100- and 1,000-fold in water, and spotted on SD (-LT) and SD (-LTHA) plates to examine growth. **b**, Venn diagram summarizing yeast two hybrid assays of meiotic proteins that interact with HCR1/PPX1 and the PP4R3A EVH1 domain. **c**, A schematic model of Arabidopsis PP4 holoenzyme complex that recognizes target protein HEI10 for dephosphorylation via the PP4R3A EVH1 domain and PPX1.

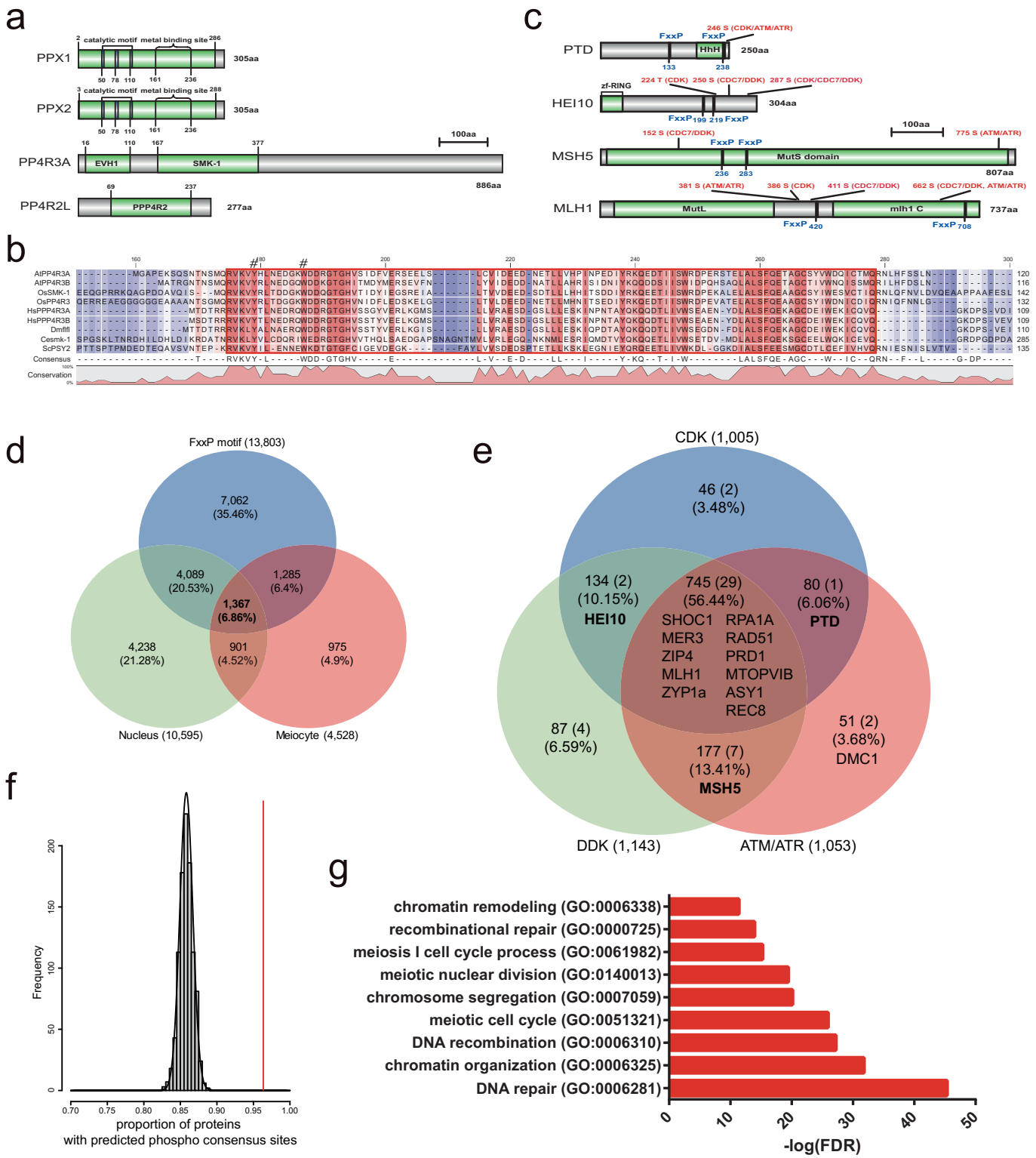

Extended Data Fig. 10 | Genome-wide prediction of PP4 complex target proteins during meiosis. a, Protein domain (green) structure of Arabidopsis PP4 subunits PPX1, PPX2, PP4R2 and PP4R3. **b**, Amino acid alignment of the PP4R3A homolog EVH1 domain (red box). Hash symbols (#) indicate conserved tyrosine (Y) and tryptophan (W) residues. **c**, As for a, but showing the positions of FxxP motifs and phosphorylation consensus sites in PTD, HEI10, MSH5 and MLH1. **d**, Venn diagram showing overlap of meiotically expressed, nuclear proteins with FxxP motifs. **e**, Venn diagram showing overlap of candidate PP4 target proteins with CDK, DDK or ATM/ATR kinase consensus motifs, predicted using GPS 5.0. The location of HCR1 Y2H interactors are indicated within the Venn diagram. **f**, Histogram showing a significant enrichment of proteins containing phosphorylation sites in the predicted 1,367 PP4 targets, compared to 1,000 sets of randomly chosen genes (n=1,367). The vertical red line indicates observed predicted PP4 target proteins containing phosphorylation sites, compared to the random sets (black lines). **g**, Gene ontology (GO) enrichment analysis of the predicted PP4 targets, using PANTHER (http://pantherdb.org/). Benjamini-Hochberg False Discovery Rate (FDR) correction was used for enrichment test.

nature research

Corresponding author(s): Ian R Henderson
Kyuha Choi

Last updated by author(s): Jan 13, 2021

Reporting Summary

Nature Research wishes to improve the reproducibility of the work that we publish. This form provides structure for consistency and transparency in reporting. For further information on Nature Research policies, see our Editorial Policies and the Editorial Policy Checklist.

Statistics

For all statistical analyses, confirm that the following items are present in the figure legend, table legend, main text, or Methods section.

n/a	Confirmed	
☐	☒	The exact sample size (*n*) for each experimental group/condition, given as a discrete number and unit of measurement
☐	☒	A statement on whether measurements were taken from distinct samples or whether the same sample was measured repeatedly
☐	☒	The statistical test(s) used AND whether they are one- or two-sided *Only common tests should be described solely by name; describe more complex techniques in the Methods section.*
☒	☐	A description of all covariates tested
☐	☒	A description of any assumptions or corrections, such as tests of normality and adjustment for multiple comparisons
☐	☒	A full description of the statistical parameters including central tendency (e.g. means) or other basic estimates (e.g. regression coefficient) AND variation (e.g. standard deviation) or associated estimates of uncertainty (e.g. confidence intervals)
☐	☒	For null hypothesis testing, the test statistic (e.g. *F*, *t*, *r*) with confidence intervals, effect sizes, degrees of freedom and *P* value noted *Give P values as exact values whenever suitable.*
☒	☐	For Bayesian analysis, information on the choice of priors and Markov chain Monte Carlo settings
☒	☐	For hierarchical and complex designs, identification of the appropriate level for tests and full reporting of outcomes
☐	☒	Estimates of effect sizes (e.g. Cohen's *d*, Pearson's *r*), indicating how they were calculated

Our web collection on statistics for biologists contains articles on many of the points above.

Software and code

Policy information about availability of computer code

Data collection	Computer code used are primarily custom R scripts (version 4.2) and CellProfiler (version 4.07).
Data analysis	Data analysis was performed using custom R scripts (version 4.2), SHOREmap, TIGER and imageJ.

For manuscripts utilizing custom algorithms or software that are central to the research but not yet described in published literature, software must be made available to editors and reviewers. We strongly encourage code deposition in a community repository (e.g. GitHub). See the Nature Research guidelines for submitting code & software for further information.

Data

Policy information about availability of data

All manuscripts must include a data availability statement. This statement should provide the following information, where applicable:

- Accession codes, unique identifiers, or web links for publicly available datasets
- A list of figures that have associated raw data
- A description of any restrictions on data availability

There are no restrictions on data availability. The raw data measurements associated with fluorescent crossover measurement and cytology are provided in the Supplementary Information. DNA sequencing files (fastq files) have been publically uploaded to the Experiment ArrayExpress accession: E-MTAB-9621
Title: Identifying crossover locations in an Arabidopsis thaliana
meiMIGS-PPX1-PPX2 Col x Ler F2 population using genotyping by sequencing

Field-specific reporting

Please select the one below that is the best fit for your research. If you are not sure, read the appropriate sections before making your selection.

☒ Life sciences ☐ Behavioural & social sciences ☐ Ecological, evolutionary & environmental sciences

For a reference copy of the document with all sections, see nature.com/documents/nr-reporting-summary-flat.pdf

Life sciences study design

All studies must disclose on these points even when the disclosure is negative.

Sample size	Sample sizes were chosen based on previous work using these techniques known to reveal significant differences between mutants and other genetic backgrounds in previous studies.
Data exclusions	No data were excluded from analysis.
Replication	In response to the reviewers concerns about growth conditions the GBS experiment has been replicated entirely in South Korea. We also provide data collected in Cambridge and South Korea to rule out significant differences in growth conditions influencing recombination.
Randomization	Plants were randomly positioned in our growth chambers.
Blinding	Blinding was not performed.

Reporting for specific materials, systems and methods

We require information from authors about some types of materials, experimental systems and methods used in many studies. Here, indicate whether each material, system or method listed is relevant to your study. If you are not sure if a list item applies to your research, read the appropriate section before selecting a response.

Materials & experimental systems

n/a	Involved in the study
☐	☒ Antibodies
☒	☐ Eukaryotic cell lines
☒	☐ Palaeontology and archaeology
☒	☐ Animals and other organisms
☒	☐ Human research participants
☒	☐ Clinical data
☒	☐ Dual use research of concern

Methods

n/a	Involved in the study
☒	☐ ChIP-seq
☒	☐ Flow cytometry
☒	☐ MRI-based neuroimaging

Antibodies

Antibodies used	ASY1, RAD51, ZYP1 and MLH1 antibodies were provided as gifts by Prof Chris Frankin and Prof Mathilde Grelon and appropriate references cited. For immunoprecipitation experiments the following antibodies were used: anti-HA (Roche 12013819001) or anti-Myc (Santa Cruz sc-9E10).
Validation	The ASY1, RAD51, ZYP1 and MLH1 antibodies have been extensively published and validated in the literature, the relevant papers have been cited in the manuscript. The HA and Myc antibodies were used according to manufacturer's instructions and were validated via appropriate negative controls.